POLITECNICO
MILANO 1863

SCUOLA DI INGEGNERIA INDUSTRIALE
E DELL'INFORMAZIONE

Positron interferometry:
towards the study of microwave influence

TESI DI LAUREA MAGISTRALE IN
ENGINEERING PHYSICS - INGEGNERIA FISICA

Author: **Federico Marsegan**

Student ID: 10561073
Advisor: Prof. Rafael Ferragut
Academic Year: 2021-22

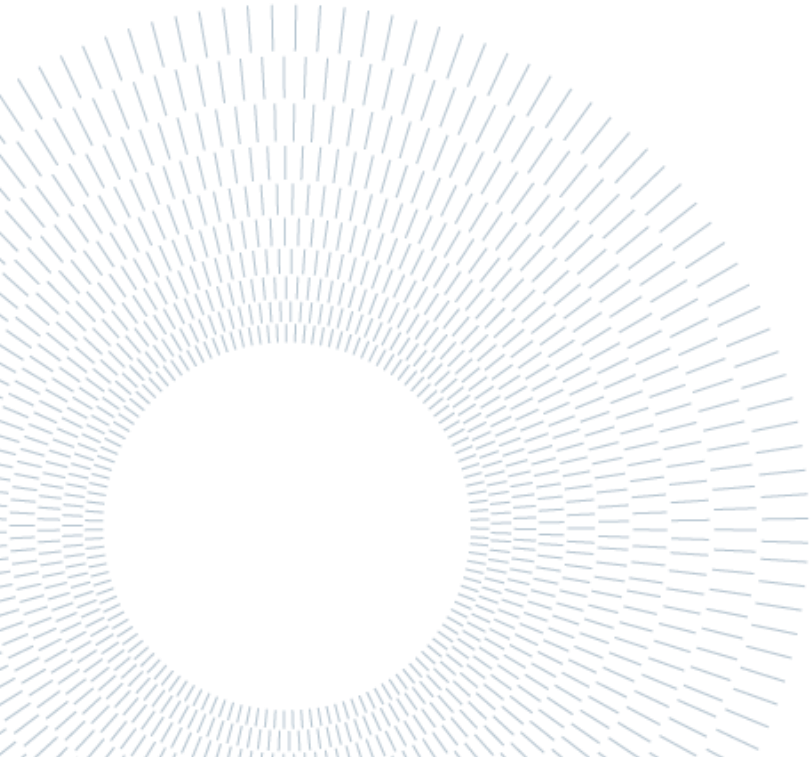

Abstract

The topic of gravitational interactions of antimatter has recently attracted a large interest in the scientific community.

This thesis is inserted in this scenario of fundamental physics. In particular, it is part of the QUPLAS project, which have the final and ambitious goal of measuring the gravitational interaction between matter and antimatter. However, the short-term goal of the project is the study of matter-wave interference of an antimatter particle, the positron. This is fundamental in paving the way for future steps towards the gravitational study.

The goal of this work is to prepare an experiment to study the interference of positrons and the effect of a perturbation, consisting in a micro-wave field. This is expected to have an influence on the phase of the positron and therefore on the interference pattern. The main goal of the thesis is the experimental implementation of the whole setup in order to perform a first campaign of measurements.

The activity took place in the L-NESS laboratory of Como (Politecnico di Milano).

Keywords: antimatter experiment; interferometry; micro-waves cavity; quantum coherence; QUPLAS.

Abstract in italiano

Il tema delle interazioni gravitazionali dell'antimateria ha recentemente suscitato un grande interesse nella comunità scientifica.

Questa tesi si inserisce in questo scenario di fisica fondamentale. In particolare, fa parte del progetto QUPLAS, che ha l'obiettivo finale e ambizioso di misurare l'interazione gravitazionale tra materia e antimateria. Tuttavia, l'obiettivo a breve termine del progetto è lo studio dell'interferenza materia-onda di una particella di antimateria, il positrone. Questo è fondamentale per aprire la strada a futuri passi verso lo studio della gravitazione.

L'obiettivo di questo lavoro è preparare un esperimento per studiare l'interferenza dei positroni e l'effetto di una perturbazione, consistente in un campo di micro-onde. Si prevede che questo abbia un'influenza sulla fase del positrone e quindi sul pattern di interferenza. L'obiettivo principale della tesi è l'implementazione sperimentale dell'intero setup al fine di eseguire una prima campagna di misure.

L'attività si è svolta presso il laboratorio L-NESS di Como (Politecnico di Milano).

Parole chiave: antimateria; interferometria; cavità microonde; coerenza quantistica; QUPLAS.

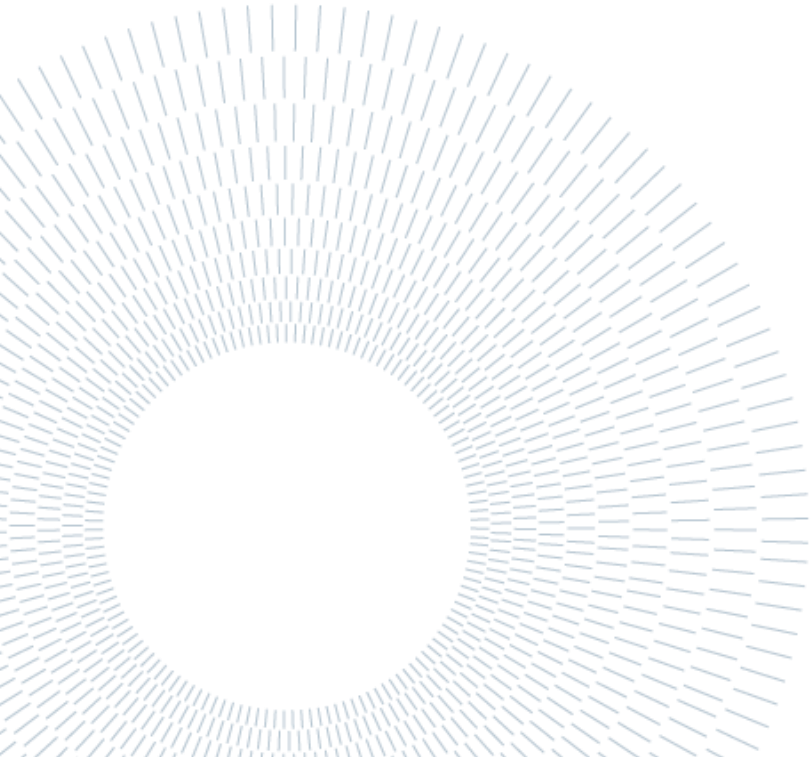

Contents

1 Introduction to the QUPLAS project

This thesis work is part of the project called QUPLAS, which stands for *QUantum interferometry, decoherence and gravity with Positron, positronium and LASers*. QUPLAS is a collaboration between different institutions [1]. The main goal of this project is the study of the interferometric and gravitational properties of antimatter. QUPLAS is divided into three phases:

- QUPLAS-0: the goal of this part is the observation of interference of positrons in a Talbot- Lau interferometer.
- QUPLAS-I: the next step consists in the observation of interference of positronium (Ps), again in a Talbot-Lau configuration. This can give experimental access to several properties of this peculiar system.
- QUPLAS-II: the final goal of the project is the measurement of the gravitational acceleration g_{Ps} of Positronium atoms by means of a Mach-Zehnder interferometer.

The experiment of interferometry with antimatter was performed in our lab in 2019 and for the first time an interference pattern was observed [2]. This was selected, by a group of Physics World editors, as part of the top 10 breakthrough experiment of 2019, all around the world. The relevance of this experiment is related to the fact that it proposes to reveal the particle-wave duality and test the fundamental laws of quantum mechanics with single antimatter particle.

QUPLAS is a big project; besides the three incremental steps, there are a lot of transitional experiments and goal to achieve. QUPLAS-0 is just the starting point and paves the way to other intermediate experiments; in the context of the antimatter waves interferometry, an evolution of this experiment is proposed, the so-called *Quantum revival experiment*, which involves the interaction of a system showing quantum properties with a particular external perturbation. For this reason, there will be an upgrade of the system concerning QUPLAS-0.

Other intermediate experiments are the Aharonov-Bohm experiment with positrons [3], the production of positronium starting from positrons, the interferometric studies on neutral antimatter systems, such as positronium. All these experiments

lead to the final ambitious goal of QUPLAS, which is to measure the gravitational acceleration of a particle of antimatter.

1.1. CPT Symmetry

One of the goals of the QUPLAS project is to verify the CPT symmetry; this means the invariance of the system under the combined action of the charge conjugation (C), parity (P) and time reversal (T) operators (Figure 1.1). Such symmetry implies the identity of lifetime and mass, but opposite magnetic moment for particles and antiparticles.

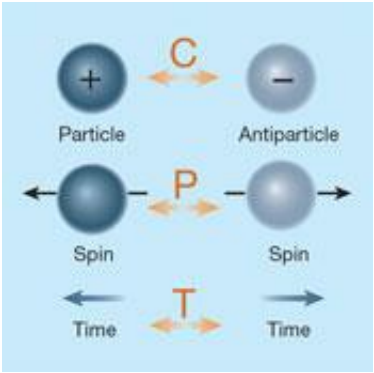

Figure 1.1: scheme of CPT symmetry [4].

CPT theorem states that every locally Lorentz-invariant quantum field theory described by a Hermitian Hamiltonian respects such CPT symmetry [4].

Thus, a break in CPT symmetry leads to a violation of Lorentz invariance. Since such invariance is the base for the physical theories developed in the 1900s, the discovery of this symmetry breaking would be quite problematic. CPT symmetry states that if two of the components are inverted, then the third must also be inverted.

Some notable examples of matter-antimatter asymmetry in specific discrete properties (P,CP,T) were found, while keeping the full CPT invariance intact [5]. As of today, CPT invariance is one of the main properties of the Standard Model and it is an argument that remains a hot topic of research.

The innovative idea of QUPLAS is to experimentally test the CPT symmetry by a quantum interferometry experiment that directly compares the quantum pattern of a fermion, the electron, and its anti-fermion, the positron.

1.2. Weak Equivalence Principle

Among the fundamental forces - electro-magnetic, gravitational, weak nuclear and strong nuclear – only the gravitational is not yet described by a quantum theory. Indeed, gravity is described by Einstein's General Relativity [6], which is a classical theory with a geometrical framework. One of the milestones of General Relativity is the Weak Equivalence Principle (WEP). The principle states that the trajectory of a free-falling body depends only on the initial position and the velocity of the body and not on its composition. From a Newtonian point of view, this means that the acceleration doesn't depend on the mass of the body; this is possible only when the inertial mass is equal to the gravitational mass of the body. The WEP was tested for matter-matter systems, with a precision of 10^{-13} by Eotvos-type experiment [7]. But this was never tested on antimatter-matter systems. A precise measurement of g could give information about the best quantum mechanical model to describe gravity.

Since the final goal of QUPLAS project is to measure the acceleration of gravity for an antimatter system, then it is strictly related to testing the WEP.

Even if a violation of the WEP is verified, it would be consistent with the CPT symmetry; indeed, the CPT symmetry predicts the behavior of an anti-apple falling on an anti-Earth, but it does not predict the behavior of anti-apple on Earth.

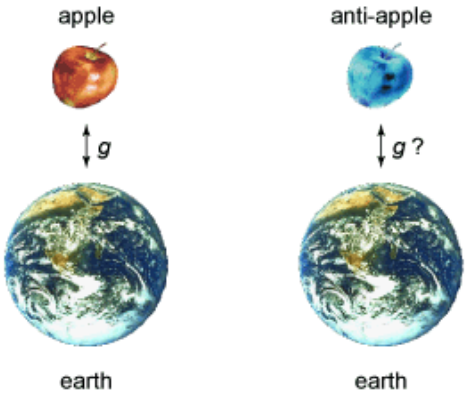

Figure 1.2: sketch of the effect of gravity on antimatter.

1.3. Positron

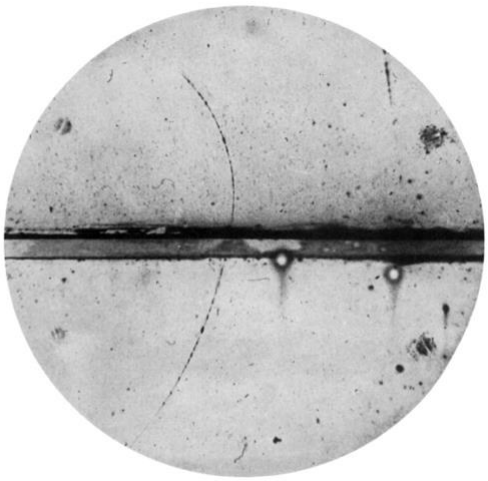

Figure 1.3: first trace left by a positron (1933) [8]

In the late 1920s, soon after the formulation of the Schrodinger Equation [9], many physicists strove to reconcile the new quantum theory with the already well-known Special Relativity, formulated by Einstein in 1905 [10]. It was Paul Dirac the one who formulated a relativistic equation of the electron.

Beside this, Dirac theorized the existence of a particle akin to the electron in mass and intrinsic angular momentum, but with positive charge [11]. Experimental detection of the positive electron, called positron, was a major goal of physics in the early 1930s, and in 1933 Carl Anderson succeeded [8].

1.4. Interferometry

Interferometry is a phenomenon where two coherent waves are superimposed resulting in a wave of different amplitude, depending on their relative phase and frequency.

This phenomenon is observed, for example, for the whole electromagnetic spectrum. However, an interferometric experiment can be performed also for matter; indeed, the premise of an experiment of interferometry is the particle-wave duality, which states that the quantistic constituents of matter (and anti-matter) have both an undulatory nature and a corpuscular nature. Which one of the two is revealed depends on the kind of experiment. This is exactly as the case of light, where in the Young experiment with the double slits [12] the undulatory nature is revealed while in the Compton experiment [13] the corpuscular one is shown. An analogous behavior is observable for electrons. We can think for example at the curios case of the Thomson father and son: the father received the Nobel prize for

demonstrating the behavior of the electron as a particle, while his son for showing its undulatory nature.

So, interferometry is a powerful way for demonstrating the principle of the particle-wave duality.

Before QUPLAS-0 no experiments have ever been carried out using particles of antimatter. Thus, QUPLAS stands as the progenitor of all antimatter quantum interference experiments. On a theoretical level a similar behavior for electrons and positrons is expected for CPT symmetry (discussed in 1.1).

In 2019 an experiment of interferometry using positron has been performed for the first time showing interesting results: an interference pattern was revealed, proving the particle-wave duality also for antimatter.

Now we enter in the detail of the matter-wave interferometry, presenting some of the theory behind it.

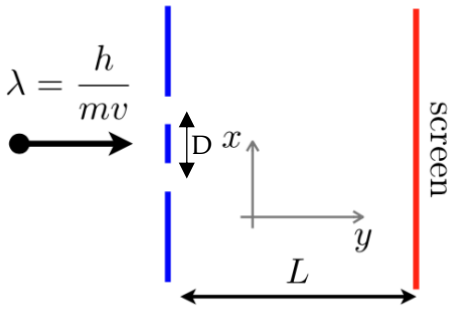

Figure 1.4: schematic representation of Young like experiment.

Consider the single point-like particle travelling with a velocity v towards a screen with 2 apertures (Figure 1.4). This is the quantum-mechanical analogous of the Young experiment with two slits and can be generalized to the more complex case of the diffractions gratings with N slits. The goal of this discussion is to understand the position distribution of the particles at the detector. One important experiment provides an answer to this problem. In 1974 a team at University of Bologna observed for the first time interference of single electron waves from an analogous of the double slit [14]. The effect of interference is the appearance of a fringe pattern in the position distribution of electron waves at the detector, proving that a true quantum interference effect was being observed without any influence of electron-electron interactions.

From the particle-wave duality, we can state that a particle shows a wave-like behavior with a de Broglie wavelength calculated as:

$$\lambda = {}^{h}/_{p} \tag{1.1}$$

If we go back to our single particle, this has momentum $p = \sqrt{2mE}$, wavefunction $\psi(x)$ and impinges on a double slit. The propagation of this particle is described by the Schrödinger equation, assuming that the energy E of the particle is weakly perturbed during propagation:

$$\nabla^2\psi(x) + k_{dB}^2[1 - V/E]\psi(x) = 0 \tag{1.2}$$

where $k_{dB}^2 = 2\pi/\lambda_{dB}$ is the de Broglie wavenumber and V is the potential. On the other hand, it is well known [15, 16] that diffraction of a monochromatic scalar field $u(x)$ is described by the Helmholtz equation:

$$\nabla^2 u(x) + k^2 n^2(x) u(x) = 0 \tag{1.3}$$

where k is the wave number and $n(x)$ is the refractive index. Comparing equations $\nabla^2\psi(x) + k_{dB}^2[1 - V/E]\psi(x) = 0$ (1.2) and $\nabla^2 u(x) + k^2 n^2(x) u(x) = 0$ (1.3), it is clear that u and ψ satisfy the same equation, where the potential term $n^2(x) = [1 - V/E]$ plays the role of a *refractive index* for the quantum object. Finally, the measured quantity in the classical case is the intensity distribution of the diffracted light and is in the quantum case the position distribution of the particles. Both quantities are proportional to the square modulus of u and ψ respectively:

$$I_{class.}(x) \propto |u(x)|^2 \tag{1.4}$$

$$I_{quant.}(x) \propto |\psi(x)|^2 \tag{1.5}$$

This is a formal analogy and allows us to adopt classical optics to model quantum interference, with different meaning of the quantity involved.

The particle travelling along y and interacting along x (Figure 1.4) with N slits can be written as a superposition of states:

$$\psi^{(N)}(x, t = 0) \sim \sum_{n=1}^{N} \psi_n(x, t = 0) \tag{1.6}$$

where $\psi_n(x, t)$ (with $n = 1, \ldots, N$) is the wave function describing the particle passing through the n-th slit and $\psi_n(x, t) = \psi_0(x - nD, t)$ is valid since the grating has periodicity D. We can think that the particle propagates unperturbed along x and is therefore governed by the free Hamiltonian:

(1.7)

$$H_{eff} = \frac{p_x^2}{2m}$$

The evolution of the state $\psi(x,t)$ is obtained solving the Schrödinger equation. In particular, the probability density distribution along the x-axis on the screen at position $y = L$ is given by $I(x) = \left|\psi^{(N)}(x, t = L/v)\right|^2$, with:

$$\psi^{(N)}(x, t = L/v) = \frac{1}{\sqrt{i\lambda L}} \int_{-\infty}^{\infty} \exp\left[i\frac{\pi}{\lambda L}(x - x')^2\right] \psi^{(N)}(x', 0)dx' \tag{1.8}$$

which is nothing but the Fresnel integral of classical optics, as expected from the analogy we established [16].

Now we can conveniently assume that the initial wavefunction has a Gaussian shape [17, 18, 19]:

$$\psi_n(x, 0) = C_n \exp\left[\frac{(x - nD)^2}{4\sigma^2}\right] \tag{1.9}$$

where $\sigma = {}^{a}/_{2\sqrt{2\pi}}$, with a the width of the slit. Now we analyze for simplicity the interference pattern generated by two slits. Assuming a gaussian wavefunction and applying the following substitution $\hat{x} = x/\sigma$, $\widehat{D} = D/\sigma$, $\hat{L} = L\lambda/4\pi\sigma^2$, we can rewrite the integral (1.8) as:

$$\psi^{(N)}(x, t) = \frac{1}{\sqrt{\lambda L}} \sum_{n=1}^{N} C_n \int_{-\infty}^{\infty} \exp\left[i\frac{(\hat{x} - \hat{x}')^2}{4\hat{L}}\right] \exp\left[-\frac{\left(\hat{x}' - n\widehat{D}\right)^2}{4}\right] dx' \tag{1.10}$$

In the case of $N = 2$, we solve the integral between $-\frac{\widehat{D}}{2}$ and $\frac{\widehat{D}}{2}$:

$$\psi^{(2)}\left(\hat{x}, \hat{L}\right) = \sum_{n=1,2} C_n \exp\left[-\frac{(\hat{x} - \widehat{x_n})^2}{4\left(1 + \hat{L}^2\right)}\left(1 - i\hat{L}\right)\right] \tag{1.11}$$

The figure of interference is given by:

$$I\left(\hat{x}, \hat{L}\right) = \left|\psi^{(2)}\left(\hat{x}, \hat{L}\right)\right|^2, \tag{1.12}$$

Therefore, substituting $F_{\pm} = \exp\left[-\frac{(\hat{x} \pm \widehat{D}/2)^2}{2(1+\hat{L}^2)}\right]$ and $C_1 = C_2$, we obtain:

(1.13)

$$I(\hat{x},\hat{L}) = F_+ + F_- + 2\sqrt{F_+F_-}\cos\left[\frac{\hat{x}\hat{D}\hat{L}}{2(1+\hat{L})^2}\right]$$

The oscillating term shows the interference component. From Figure 1.5, we see the behavior of $I(x,y)$.

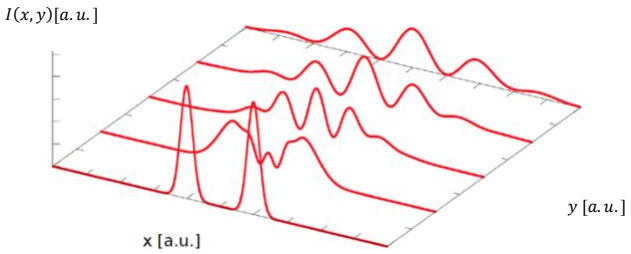

Figure 1.5: probability of finding the particle as a function of the distance y.

1.4.1. General Talbot-Lau configuration

To perform an experiment of interferometry with positrons a particular configuration of the interferometer should be adopted. In QUPLAS-0 the experiment was performed using an asymmetric Talbot-Lau configuration [20]. It consists in a magnifying setup for the direct detection of the interference fringes with nuclear emulsion detector.

Considering the five-six order of magnitude separating the typical transit time through the interferometer (10 ns) and the average time distance between consecutive positrons (1-10 ms) a single particle experiment is realized. In this regime any interaction between interfering particle can be neglected.

Now we start with the description of the general (symmetric) Talbot-Lau interferometer. It is constituted by two gratings (G_1, G_2), as schematized in Figure 1.6. The first grating generates a series of wavefronts which are coherent at the second grating. So, it is responsible for generating coherence. The effect of the second grating is to produce the interference pattern that will be measured at the detector.

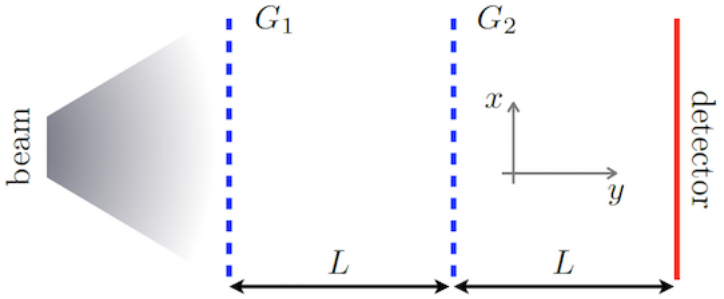

Figure 1.6: general scheme of a Talbot-Lau interferometer.

Talbot-Lau interferometer exploits two effects: self-imaging Talbot effect and Lau effect. The first is responsible of the formation of the image of the grating transfer function at a distance $L = nT_L$ (with $n = 1, 2, 3, ...$) from the first grating, where T_L (Talbot length) is defined as:

$$T_L = D^2/\lambda \tag{1.14}$$

with D the periodicity of the grating and λ the positron wavelength.

The Lau effect [21] regards the constructive superposition at the second grating of the image produced by the first grating and the periodicity of the second one. This happens only if a condition is satisfied: the distance between the first and the second grating must be the same distance between the second grating and the detector and equal to $L = nT_L$ (with $n = 1, 2, 3, ...$). Moreover, the two gratings must have the same periodicity.

This configuration has an important advantage; allows to exploit an incoherent particle beam to perform experiment of interferometry.

From Figure 1.8, we can understand why a Talbot-Lau interferometer is needed for experiment in which partially coherent waves are considered. In Figure 1.7 (left) plane waves impinging onto one grating generate an interference pattern which is periodically visible in space, in multiples of the Talbot length T_L. In the case of incoherent or partially coherent illumination (Figure 1.7 (right)) the Talbot effect is no more observed.

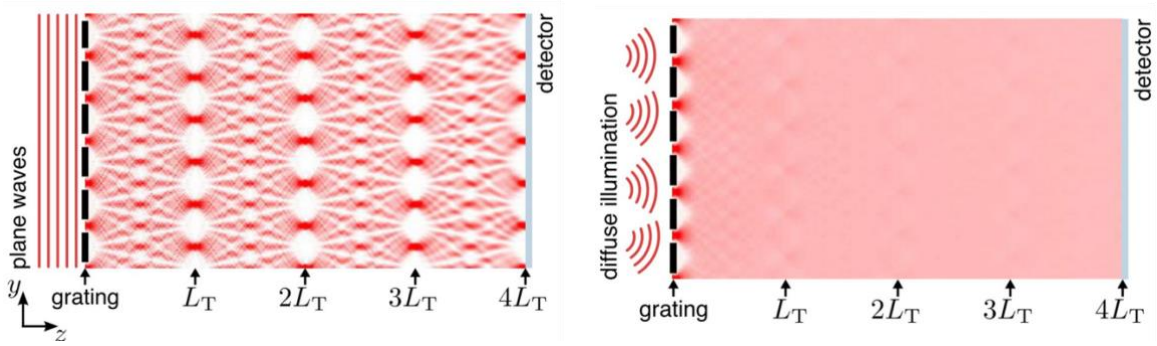

Figure 1.7: carpet of interference for different distances, for plane wave or coherent particles (left) and diffuse illumination or partially coherent particles (right), in the case of single grating.

In Figure 1.8, instead, we notice that using a second grating, also with incoherent illumination, the interference pattern appears at the detector plane.

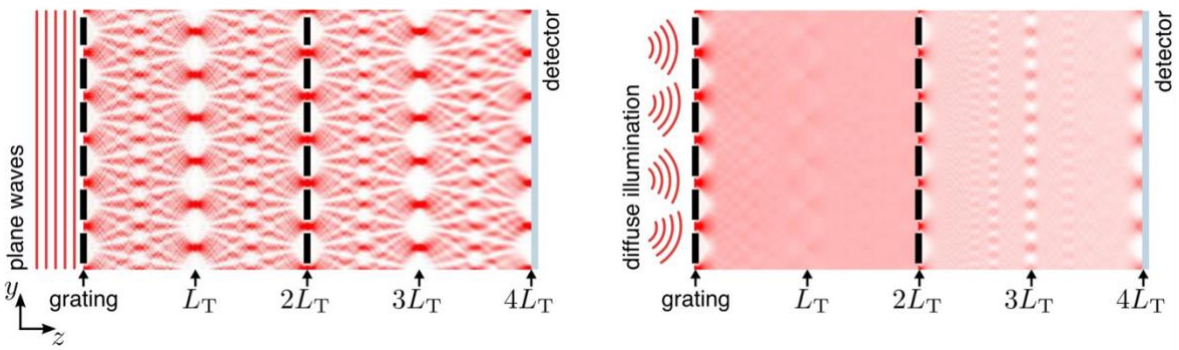

Figure 1.8: Talbot carpet (two gratings) for plane waves or coherent particles (left) and diffuse illumination or partially coherent particles (right).

Another advantage of this configuration is that the particles are weakly influenced by the external electric and magnetic field. Moreover, unlike an interferometer that works in the Fraunhofer region, in which the distance source-detector should be high ($L \gg a^2/\lambda$ with a width of the slits in the grating), a Talbot-Lau allows to minimize the dimension of the apparatus; this is a very important aspect when working with positrons [20]. Talbot-Lau offers the capability to work with low-intensity and weakly coherent beam.

1.4.2. Asymmetric Talbot-Lau

The difference of the asymmetric configuration is represented by the fact that the periodicity of the two gratings is not the same. This has the advantage of magnifying the interference pattern which becomes sufficiently large to be detected [20]. The magnification is described through the factor η, which is related to the ratio of the two gratings periods. $\eta = 1$ means no magnification and therefore $d_1 = d_2$(where

d_1 and d_2 are the periodicities of the two gratings). For $\eta > 1$ what we obtain is a magnified fringe period, given by $d_3 = \eta d_1$ [20]. The distance between the first and the second grating is $L = \frac{d_1}{d_2} L_T$, with $L_T = d_2^2/\lambda$. The detector is placed at a distance ηL from the second grating, as summarized in Figure 1.9.

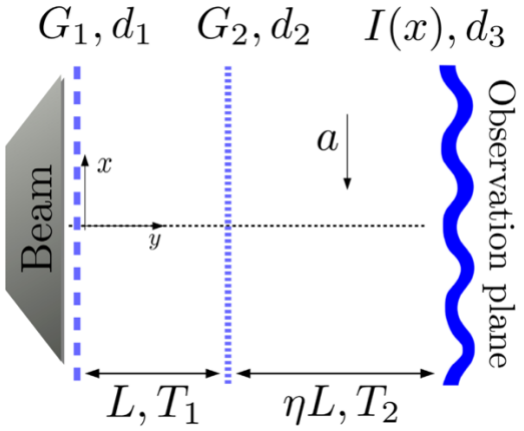

Figure 1.9: schematic representation of the asymmetric Talbot-Lau configuration.

The measured contrast expected for a Talbot-Lau interferometer is incompatible with classical moiré deflectometry [22]. A moiré deflectometer is an analogous scheme as the one showed in Figure 1.6, but particles propagate on ballistic trajectories through the gratings. The difference is that the distances $L^{(n)}$ and the periods $d^{(n)}$ are chosen to satisfy:

$$L^{(n)} \frac{\lambda}{d^{(n)}} \ll d^{(n)} \rightarrow L^{(n)} \ll L_T \tag{1.15}$$

Therefore, quantum diffraction is negligible. For this reason, a moiré deflectometer will always produce a fringe system with a larger period than the Talbot- Lau setup of the same length tuned for the same particle beam. However, the properties of the quantum and classical fringe patterns are very different. For example, in the moiré deflectometer the visibility is independent of the particle energy [23]. This is why the effects of the moiré deflectometer is considered *geometrical shadow patterns*, in contrast with the quantum interference fringes of a Talbot-Lau interferometer.

1.5. Perturbation of microwave field

The novelty of this project, compared to the previous QUPLAS-0 interferometry experiment [27] consists in an additional phase term in the positron wavefunction. The additional perturbation consists in a 10 GHz microwave stationary field, generated inside a cavity. The positron-microwave interaction produces an effect related to the undulatory nature of positrons.

Figure 1.10: image of the microwave cavity.

The standing microwave cavity will be located after the second grating. In this way, the single positron crossing the second grating will interact with photons. The amplitude of the required field varies along the perpendicular plane according to the direction of propagation of the particle (Figure 1.11), so that the different paths that the particle takes at the same time, undergo a different phase shift. This should correspond to a variation of the interference pattern position on the detector. The shift of the fringes position will depend on the phase of the field when the antiparticle enters in the cavity; nevertheless, the phase of the positron at the entrance is completely random. Therefore, a reduction in the visibility of the interference pattern is expected.

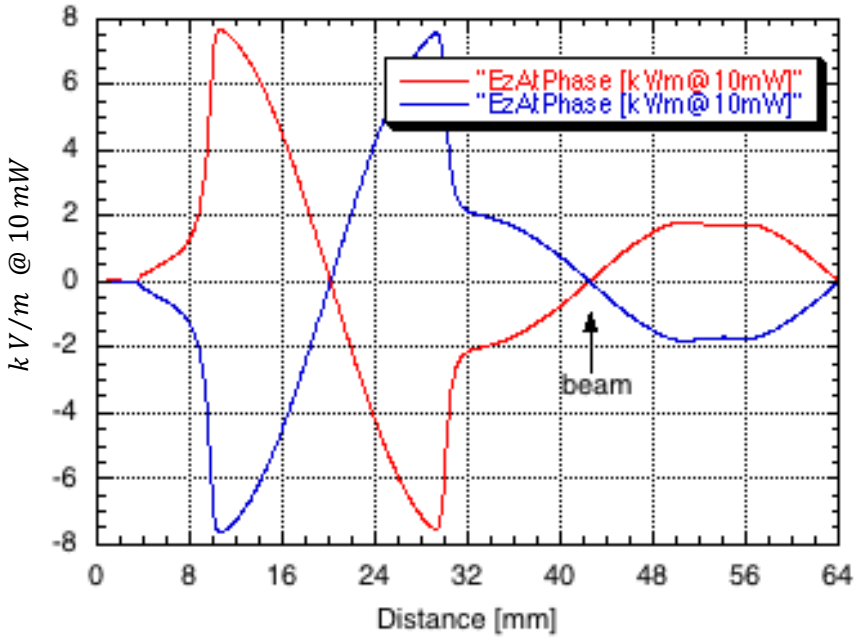

Figure 1.11: component of the electric field along the cavity.

Beyond this decoherence effect (reduction in visibility), it could be also expected a periodic variation of the visibility as increasing the electric field intensity. This effect is called *revival*. Indeed, after the decoherence explained before, a recover of coherence could be expected, consisting in an increase of visibility. This is followed by a new loss of coherence, and so on.

Therefore, the revival consists in periodically losing and recovering the coherence. As a matter of fact, for this experiment, it is proposed in the following a theoretical model, developed by S. Cialdi et al. [24], which predicts this effect, i.e. the pattern contrast of interferometry has a periodic variation as a function of the electric field intensity.

The field is externally tunable by changing the microwave power. This can lead to the first revival effect ever detected between an anti-particle and an electromagnetic field; this can demonstrate the variation of the wavefunction phase of the antiparticle due to the interaction with a microwave stationary field.

Now we analyze the theoretical description of the effect through the two slits model (also used to describe interference in Sec.1.4).

In this model, the microwave cavity is placed soon after the second grating, considered as two slits grating, as in Figure 1.12.

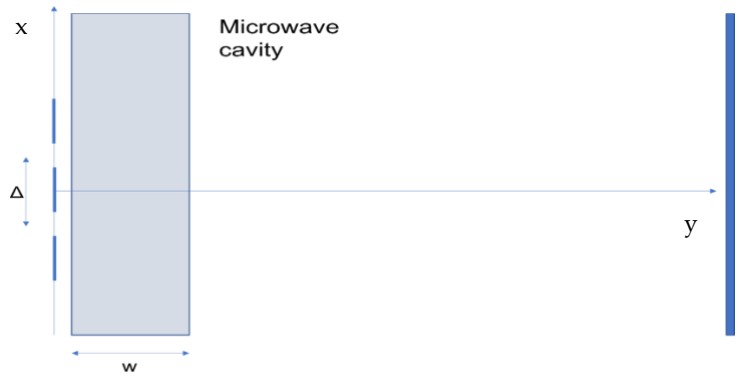

Figure 1.12: sketch of the two slits model.

The positron is propagating along y and interference occurs along x. Therefore, we can consider an eigenstate of the type $|x\rangle|p_y\rangle$ crossing a region where the vector potential is:

$$A_y = \frac{E_0}{\omega}\cos\left(\frac{\pi x}{w}\right)\sin(kx)\cos(\omega t + \phi) \tag{1.16}$$

This is the vector potential of the microwave field in the cavity of length w. The Hamiltonian of interaction between the particle and the field is:

(1.17)

$$H = -\frac{q}{m} A_y p_y$$

Considering a position at the center of the x and y axes, with $y \ll w$ and $\sin(kx) \cong kx$, we can write the potential as:

$$A_y \approx \frac{E_0}{\omega} \text{kxcos}\,(\omega t + \phi) \tag{1.18}$$

The evolution of the state along z, crossing the microwave cavity, is represented by:

$$\exp\left(-\frac{i}{\hbar}\int_0^t H(t)dt\right)|x\rangle|p_y\rangle \cong \exp\left(\frac{ip_y qE_0}{\hbar m} kx \int_0^t cos(\omega t + \phi)\, dt\right)|x\rangle|p_y\rangle \tag{1.19}$$

The particle enters the cavity with a random phase ϕ, so that, defining:

$$P(\phi) = \int_0^t \cos\,(\omega t + \phi)dt \tag{1.20}$$

$$k_x(\phi) = \frac{ip_y qE_0}{\hbar m} kP(\phi) \tag{1.21}$$

we can rewrite (1.19) in a more compact form:

$$\exp(ik_x(\phi)x)|x\rangle|p_y\rangle \tag{1.22}$$

Now we consider the effect of the two neighboring slits:

$$\begin{aligned} &\exp(ik_x(\phi)x)|x\rangle|p_y\rangle + \exp\big(ik_x(\phi)(x+\Delta)\big)|x+\Delta\rangle|p_y\rangle = \\ &= \psi_1 + \psi_2 \exp(ik_x(\phi)) \end{aligned} \tag{1.23}$$

This formalism can be used to evaluate the effect of the interaction on an already existing periodic pattern on the detector. The unperturbed (without microwave) pattern is described by:

$$\frac{1}{2}\left[1 + \cos\left(\frac{2\pi}{\lambda_T} x_q\right)\right] \tag{1.24}$$

Where x_q is the coordinate and λ_T is the observed wavelength on the emulsion detector. The effect of the microwave field is to modify the pattern introducing a phase shift:

$$f(x_q, \phi) = \frac{1}{2}\left[1 + \cos\left(\frac{2\pi}{\lambda_T} x_q - k_x(\phi)\Delta\right)\right] = \frac{1}{2}\left[q + \cos\left(\frac{2\pi}{\lambda_T}(x_q + \Delta x_q\right)\right] \tag{1.25}$$

Since the phase of the positron entering the cavity is random, one has to integrate over the possible phases (1.20):

$$g(x_q) = \frac{1}{2\pi}\int_{-\pi}^{\pi} f(x_q,\phi)d\phi = \frac{1}{2\pi}\int_{-\pi}^{\pi}\left[1+\cos\left(\frac{2\pi}{\lambda_T}x_q - k_x(\phi)\Delta\right)\right]d\phi \quad (1.26)$$

This is the new function and its visibility is plotted as a function of the microwave field in Figure 1.13.

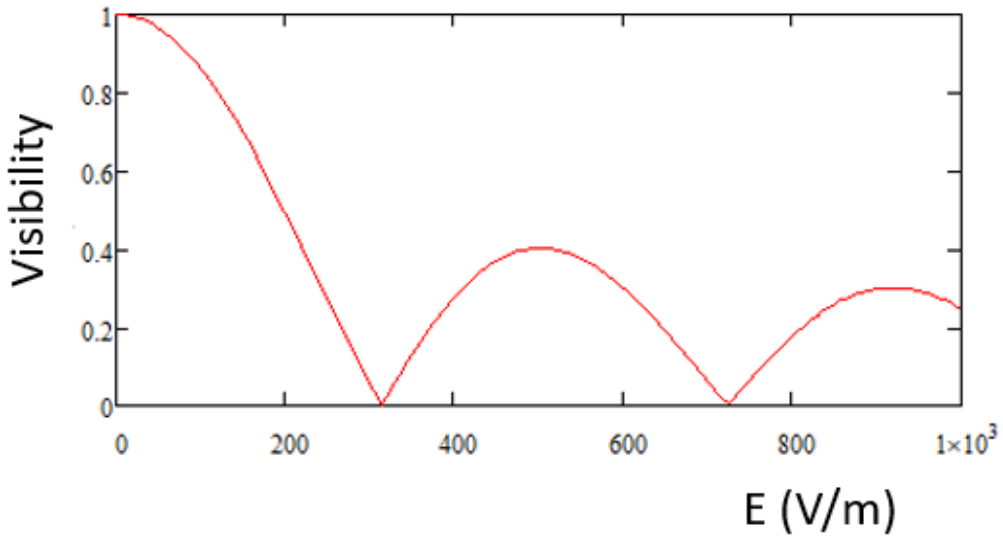

Figure 1.13: visibility as a function of the electric field in the two slits model.

1.5.1. Revival effect

The revival is an interesting quantum phenomenon, related to the particle-wave duality. The case of this thesis is not the first time that this effect has been investigated. Indeed, several experiments in the past were performed in order to observe the *quantum revival*. However, this thesis proposes to be the first investigation of this effect on an antimatter particle. This represents the novel aspect of this work.

An experiment performed in 1995 by Michael Chapman et al. [25] had the goal of investigating the revival on atoms. Starting from the atomic interference, the interaction between atoms and photons had been added in order to cause, through the single photon scattering, the "destroy" of the interference fringes [26]. In particular, it consisted in studying the fringe contrast as a function of the position of incidence of the laser. The interferometer used was a Mach-Zehnder interferometer (Figure 1.14). Single photons are scattered from atoms within a two-path atom interferometer at different locations z corresponding to different spatial separations of the interfering atom waves (Figure 1.14).

The results showed not only a loss of coherence, but also a subsequent revival of the fringe contrast. This experiment had the property that the loss of coherence can not be attributed to smearing of the interference pattern caused by momentum transferred in the scattering process but is the result of random phase shifts between the two interfering paths. The loss and regain of coherence are explained by the fact that the atomic wave function becomes entangled with that of the scattered photon [25, 26].

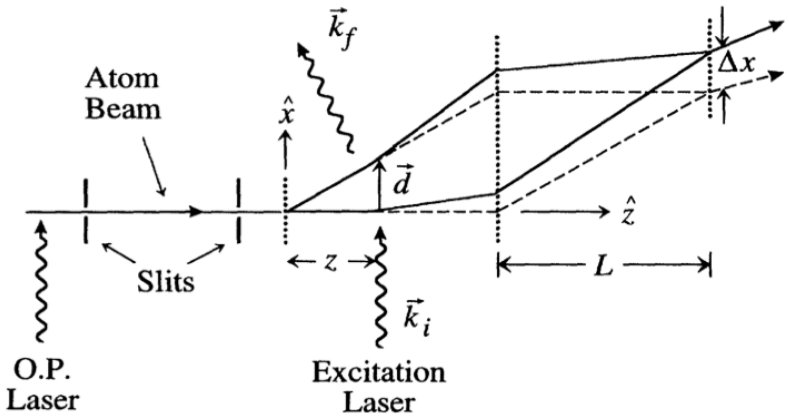

Figure 1.14: a schematic of the atom interferometer used in the experiment [25]. The original classical trajectories of the atoms (dashed lines) are altered (solid lines) due to scattering a photon (wavy lines). The atom diffraction gratings are indicated by the vertical dotted lines.

2 Experimental setup

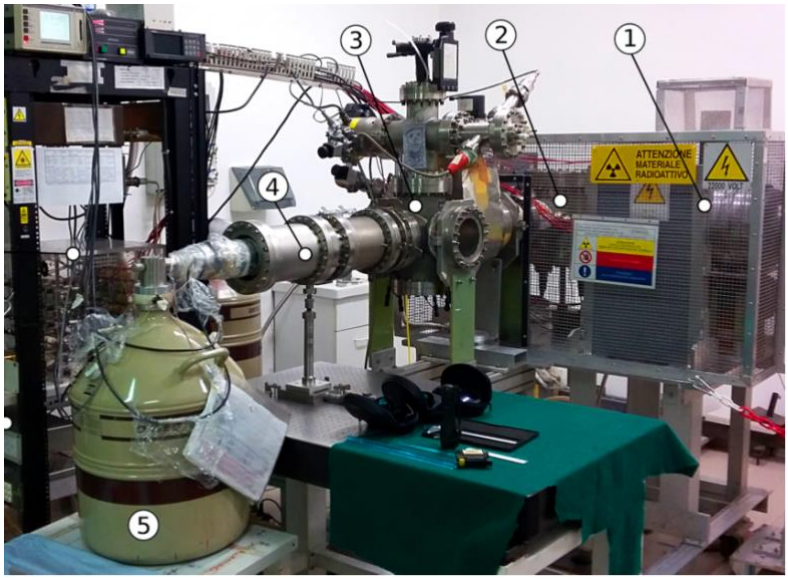

Figure 2.1: image of the experimental setup.

In Figure 2.1 we can see an image of the whole experimental setup; it is constituted mainly by two parts: the first is related to the guidance of the positron beam, the second is the part of the interferometer.

In the first part, positrons are emitted by a ^{22}Na source (1); then, they pass through the moderator, which is followed by the system of electrostatic optics (2) used to guide the beam. All is contained in a Faraday cage to protect the people from the high voltages. The chamber is divided in two regions through a mechanical valve.

To conduct the experiment of interferometry is necessary the condition of high vacuum inside the chamber. The first section, which contains the positron source and the electrostatic optics, is equipped with a two-pump system and is regularly maintained at a pressure on the order of 10^{-8} mbar. The second section includes those parts of the instrumentation that are putted in air many times to work with the beam or the interferometer. When this second sector is brought to atmospheric pressure, the valve is kept closed so that the source and the moderator, which are particularly sensitive to exposure in air, remain in high vacuum condition.

At the end of the optics (3) there is the center of the chamber, where the first grating of the interferometer (4) is mounted. A detector (5) is used to monitor the number of positrons during the interferometric experiment.

2.1. Positron source

Positrons used at L-NESS are generated by the isotope ^{22}Na, through a β^+ decay. As shown in Figure 2.2, the isotope decays in ^{22}Ne producing a positron e^+, a γ ray at 1274 keV and a neutrino ν. The decay time of the source is around 2.6 years.

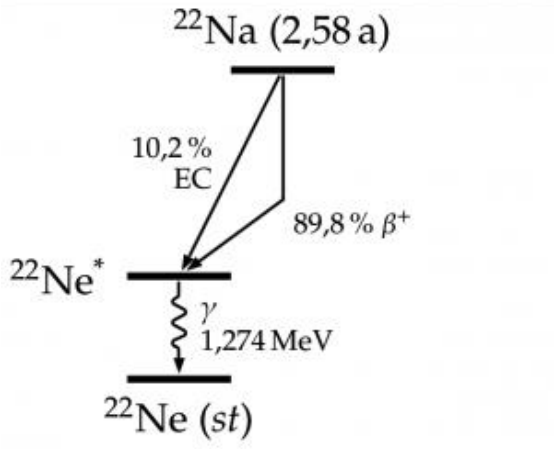

Figure 2.2: illustration of the ^{22}Na decay.

Positrons emitted have a kinetic energy characterized by a continuum spectrum from zero up to a maximum value (Figure 2.3). However, for interferometric experiments it is necessary to have a monochromatic beam. Therefore, positrons emitted by the source are made to pass through a tungsten foil which acts as a moderator.

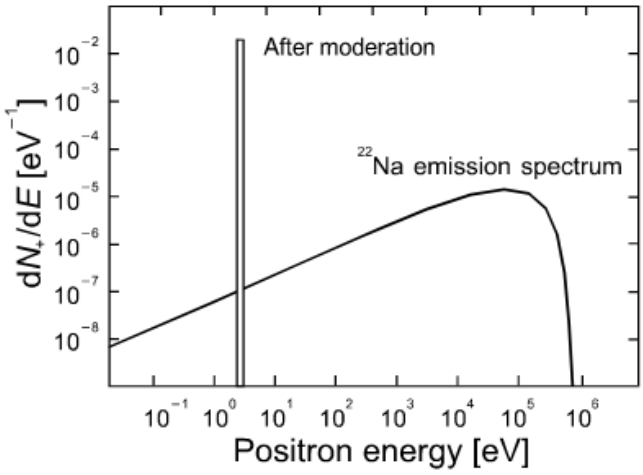

Figure 2.3: scheme of the kinetic energy of the emitted positrons.

2.2. Moderator

The effect of the moderator is to bring out a monochromatic beam of positrons (positrons with the same energy).

The moderation process is based on the fact that many solids have a negative positron work function; in this work, tungsten is picked as the material with negative work function. The work function of tungsten is around -3 eV [28].

The moderator consists in a foil of monocrystalline tungsten with orientation <100> and with thickness $1\mu m$, placed on top of the source capsule. This works in transmission geometry, in the sense that, since the thickness of the foil is much smaller than the mean positron penetration depth, only a small fraction of them thermalizes and starts to diffuse. If the surface is reached during the diffusion, the positrons are spontaneously emitted from the moderator foil with a kinetic energy equal to the work function (Figure 2.4).

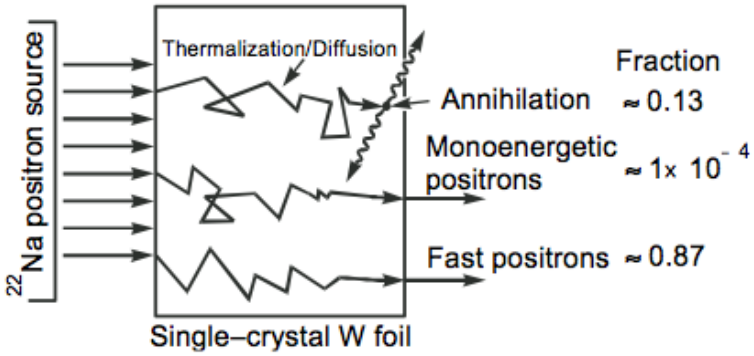

Figure 2.4: scheme of the moderation process of a positron beam.

The efficiency of this process, defined as the ratio of the number of moderated positrons over the number of incident positrons, is of the order of 10^{-4} [29]. This value is related to the fact that a fraction of the positrons (~13%) annihilates within the moderator and another (~87%) is transmitted without thermalization because it is too energetic (Figure 2.4). So, after the moderator is necessary to separate the fast positrons from the slow positrons. This will be done by the electrostatic optics (Sec. 2.3).

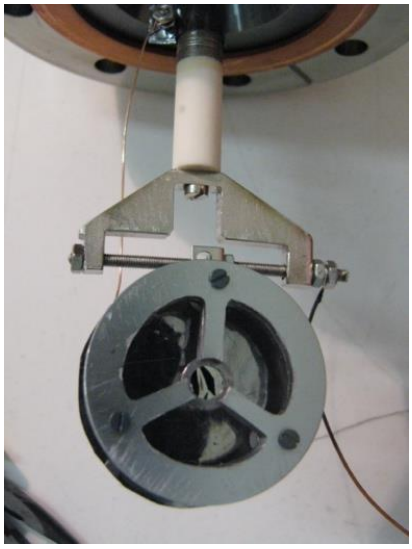

Figure 2.5: image of the moderator and its support, ready for the thermal treatment.

One problem that can alter the feasibility of the moderation process is the fact that positrons can be trapped in defects during the diffusion, therefore we need to limit as much as possible the presence of defects. To do so, the moderator must be prepared by thermal annealing [29]. With this process is possible to achieve a moderation efficiency of $3 \cdot 10^{-3}$, which means that $3 \cdot 10^{-3}$ of the total incident positron exit the moderator as monoenergetic slow positrons. Thermal treatment is essential in achieving a good moderation efficiency, indeed warming up at high temperature has a double effect:

- modifies the moderator material to be in crystalline form,
- cleans the emitting surface of oxides and other contaminants, such as carbon [29].

Crystallinity then reduces the density of crystallographic defects such as grain boundaries.

The thermal treatment consists of a series of cycles in which the temperature is increased by steps followed by a very low cool down. A slow rate of cooling is essential in order to avoid mechanical stresses that could potentially create new crystallographic defects.

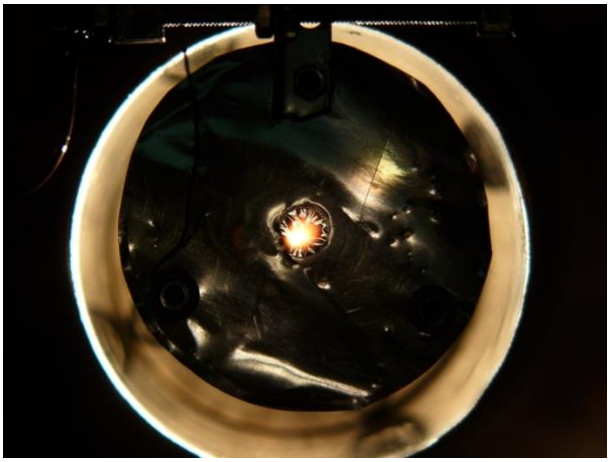

Figure 2.6: moderator at high temperature under electron bombardment.

During the thesis period the process of thermal annealing was conducted and resulted essential to improve the number of positrons necessary for the interferometric experiment.

The process used to produce an increase in temperature is called conditioning. This process was performed by electron beam bombardment, through an electron gun. The gun consisted of a tungsten filament and four electrodes each at a given potential, placed in a vacuum chamber, where it reached 10^{-8} mbar of pressure [30]. The electrons had energies in the range 1– 6 keV and were implanted on the film face opposite to that where the positrons are re-emitted, in order to reduce radiation damage and related defects close to the emitting surface. During the electron bombardment, temperature measurements of the film were made using a calibrated optical pyrometer (Impact infratherm pyrometer ISR 12-LO, which measured temperature in the range 800°-2500°). The procedure followed in this work was based on the one indicated in the paper [29]. Table 2.1 gives the operational values of the bombardment time and the approximate film temperature for six successive steps (one conditioning cycle) in our W-moderator conditioning process. In the thesis work the moderator was submitted to a total of 4 conditioning cycles.

Step #	Approximate T (°C) (±60°C)	Bombardment duration (s)
1	840	1800
2	1100	1800
3	1300	600
4	1600	100
5	1850	100
6	2100	10

Table 2.1: W-conditioning parameters employed.

After this process of moderation, a monoenergetic beam is obtained and guided by the electrostatic optics.

2.3. Optics

The fraction of positrons moderated by the tungsten foil must be separated from all the other positrons emitted at high kinetic energy. For this reason, there is the need of a guiding system, constituted by electrostatic optics, as schematized in Figure 2.7. The system is formed by two perpendicular arms, forming a L, with a series of tubes placed at certain potentials. The goal is to guide the beam.

The first part of the optics after the moderator is constituted by a series of tubes, kept ad different potentials. The moderator is kept at 1000 V in order to extract the positrons at 1keV. Then, in order to give a kinetic energy higher than 1keV, it is necessary to increase the potentials of the entire system by a constant value (the so-called HV-common). For the interferometric experiment the chosen positron kinetic energy is 14keV, which is the energy that gives the higher contrast (according to previous experiments [2], as shown Figure 2.8). The aim of the first series of electrodes is to accelerate the beam and make it parallel.

The most important part is the so-called *bender* (located in the 90° curve in Figure 2.7), which is a system of 7 parallel plates, kept at crescent potentials from the inside to the outside. The task of this part of the optics is to eliminate the "fast" positrons, those not moderated and so with high kinetic energies. The structure and the potentials of the plates guarantee that only the moderated positrons (with the correct kinetic energy) follow the parabolic trajectory and continue the propagation in the following tubes. The other positrons are removed from the beam and annihilate elsewhere.

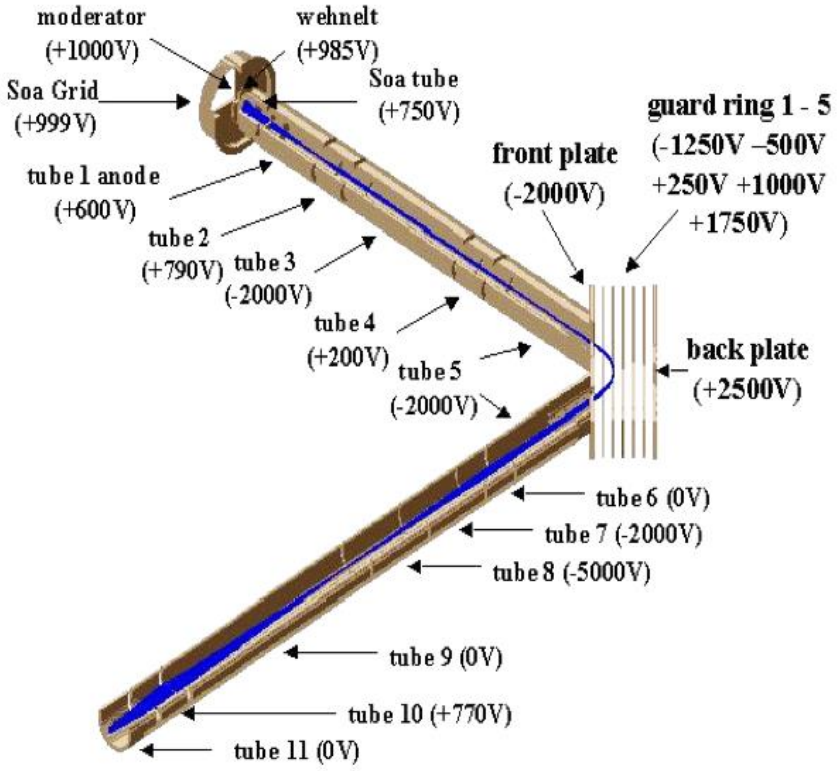

Figure 2.7: representation of all the part (with relative voltage) of the electrostatic optics.

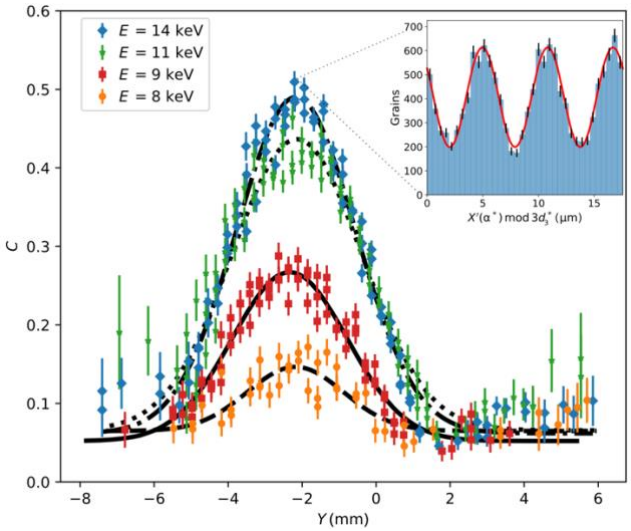

Figure 2.8: contrast obtained for different energies. The maximum is achieved with 14 keV [2].

Of particular importance is the tube 5. This tube contains defection plates, which are schematized in Figure 2.9. These deflection plates allow to have control over the shape of the beam in x and y and its position before the bender. These conditions are very crucial; indeed, a good control of the beam before the "curve", allow to obtain a well-shaped beam also at the end of the optics. Tubes 6 and tubes 9, after the bender, also contains deflection plates, which allow to correct the position of the beam.

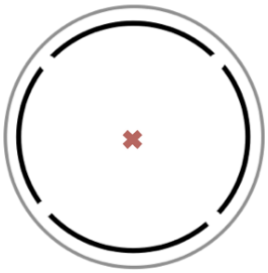

Figure 2.9: representation of a tube with the four deflection plates, that are called X-1, X-2, Y-1 and Y-2.

Another important part is the tube 10. The voltage at which is kept this electrode is the focalization voltage of the beam. Modifying this parameter, the focalization of the beam, and so the position at which is focalized, changes. This results an important parameter for the interferometric experiment and an analysis of the dimension of the beam at different focalization voltages is necessary and will be described later (Sec. 3.3).

At the end of the optics the beam is made to pass through a collimator of 2 mm of diameter and 10 cm long in order to give a better coherence to the beam before entering the interferometer.

2.4. Interferometer

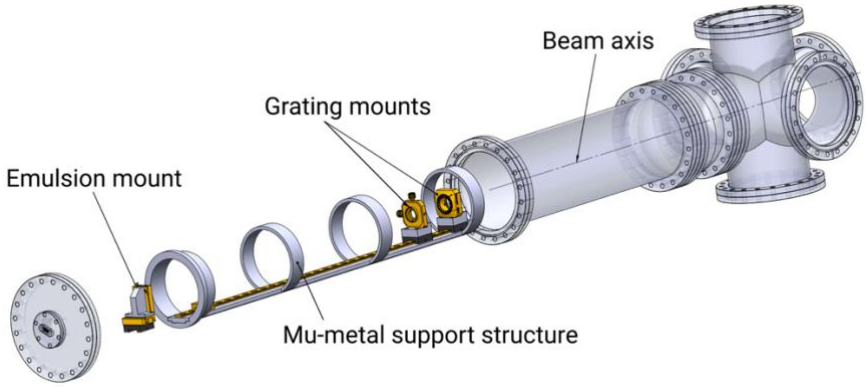

Figure 2.10: sketch of the interferometer structure and its position after the chamber.

The interferometer is an asymmetric Talbot-Lau interferometer, which was theoretically described in Sec. 1.4.2. Now the experimental implementation is discussed.

It is formed by two gratings of gold coated SiN with different periodicity and thickness $\approx 700\ nm$. It is optimized for positrons at 14 keV, with a corresponding de Broglie wavelength of 10.3 pm. The periods of the gratings are $d_1 = 1.2\ \mu m$ and $d_2 = 1\ \mu m$. The Talbot length is $T_L = d_2^2/\lambda \cong 9.7\ \mu m$ and the magnification ratio $\eta = 5$. The distance between $G1$ and $G2$ is approximately $L_1 = 118.6\ mm$. The periodicity of interference pattern at the detector is expected to be $d_3 = \eta d_1 = 6\ \mu m$. The distance L_2 should be calculated in order to give the resonance condition [20]:

$$\frac{L_1}{L_2} = \frac{d_1}{d_2} - 1 \tag{2.1}$$

And therefore $L_2 \cong 580\ mm$. At this distance from the second grating is placed the detector, which is an emulsion detector (described in detail in Sec. 2.7.1). In Table 2.2 are summarized the parameters of the interferometer chosen for the experiment.

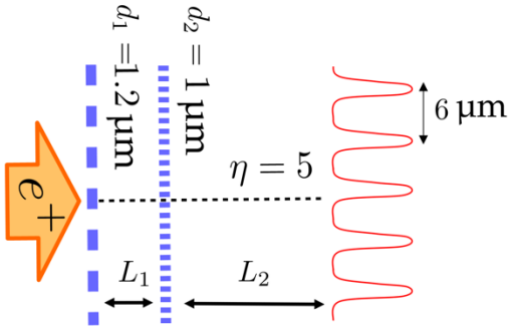

Figure 2.11: schematic representation of the chosen configuration.

d_1	E	λ	L_T	L_1	L_2	d_3
$1.2d_2 = 1.2\ \mu m$	14 keV	$1.03 \cdot 10^{-11}\ m$	$9.71\ cm$	$118\ mm$	$576\ mm$	$6\ \mu m$

Table 2.2: parameters of the interferometer.

The position of the detector is crucial; a mistake of some millimeter leads at completely losing the interference pattern. The required accuracy of the condition of (2.1) should be increased as the incoherence of the beam is approached. To improve the tolerance to possible misalignment the beam is collimated with a 2 mm wide collimator of length 10 cm (Figure 2.12).

Regardless of beam coherence, the experimental uncertainty on the ratio L_1/L_2 is around $\sigma_{L_1/L_2} = 0.002$ and stems from the errors on the measured grating periods. In the adopted geometry, this corresponds to an uncertainty of 5 mm on L_2. The brilliant idea to circumvent this problem is to place the emulsion at 45° [20].

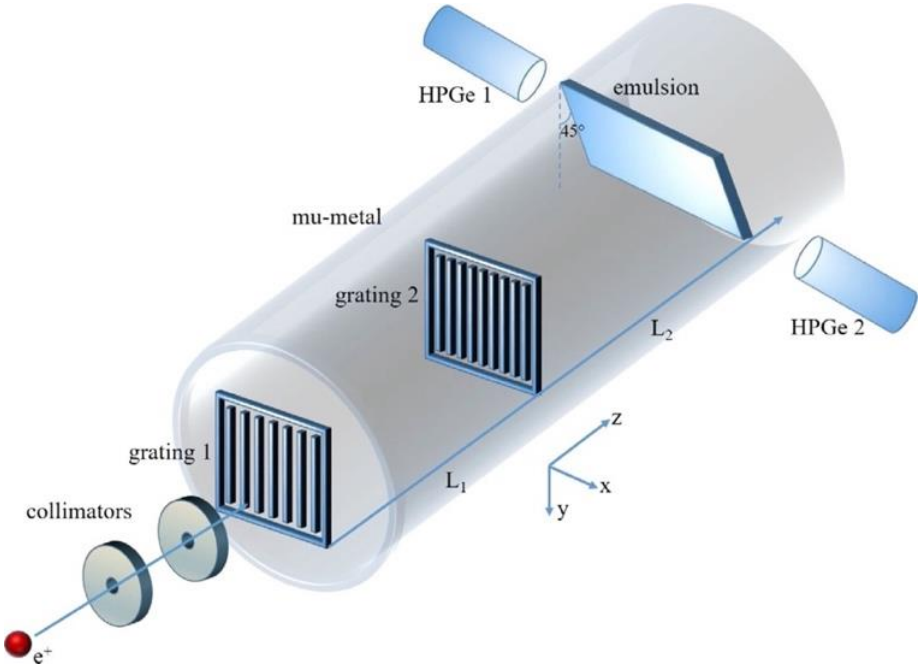

Figure 2.12: representation of the interferometer.

Another key parameter is the rotational and longitudinal alignment of the two gratings, which will be described in the next section (Sec. 2.5).

The gratings and the emulsion holder are then placed on an optical rail and inserted in the chamber (Figure 2.13).

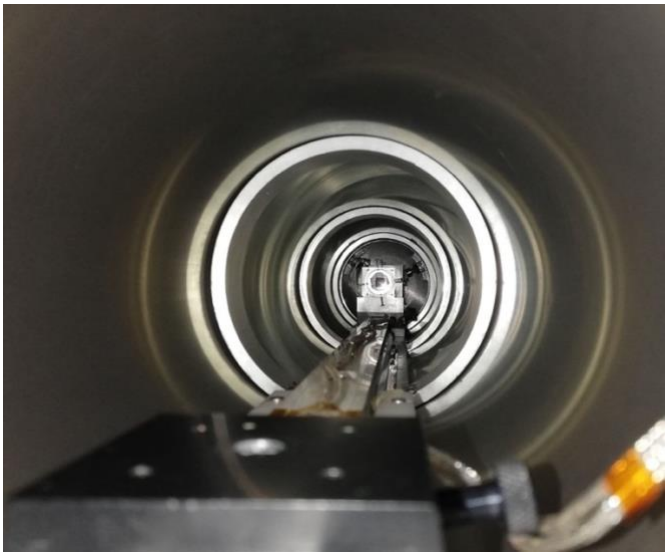

Figure 2.13: image of the interferometer from the end of the chamber. The second grating is clearly visible.

2.4.1. μ - metal

One key factor for a good success of the experiment of interferometry is that the beam should propagate inside the interferometer without being deflected or deviated. In the region of the interferometer the beam is no more guided by the electrostatic optics, therefore is completely "free". Since positron is a charged particle (anti-particle) it is influenced by the magnetic field of Earth. Knowing that the interferometer is around 70 cm it is possible to calculate the deviation of the positron beam produced by the Earth magnetic field, due to the Lorentz force:

$$\boldsymbol{F_L} = e\boldsymbol{v} \times \boldsymbol{B_E} \tag{2.2}$$

where B_E is the Earth magnetic field, in which the most important component is the vertical one (which value is 41 855.0 nT, from top to bottom). Considering that the positrons have velocity in the horizontal plane, the Lorentz force produce a deviation towards the left. Considering an arbitrary kinetic energy of 10 keV, it is possible to calculate the cyclotron radius $R = \frac{m_0 v}{eB_E} \cong 8.056\, m$. It results that in a portion of 70 cm the deviation with respect to the linear trajectory is around 2.62 cm, which could be important for the experiment (since the gratings have a dimension of 3mm x 3mm, the beam would pass completely outside the gratings).

To avoid this situation, there is the need of screening the magnetic field of Earth through the use of two cylindrical and concentric tubes of $\mu - metal$ inside the steel tube which contains the interferometer. $\mu - metal$ is a metal alloy, mainly constituted by nickel, which confers a very high magnetic permeability. The magnetic permeability is defined as: $\mu = \boldsymbol{B}/\boldsymbol{H}$ (*magnetic flux density* over *magnetic*

field intensity) and represents the magnetic conductivity of the material. The fact that μ is high means that the magnetic field lines stay confined inside the cylinders of $\mu - metal$, where the magnetic conductivity is higher. Therefore, the region inside the two concentric cylinders turns out to be screened.

2.5. Alignment

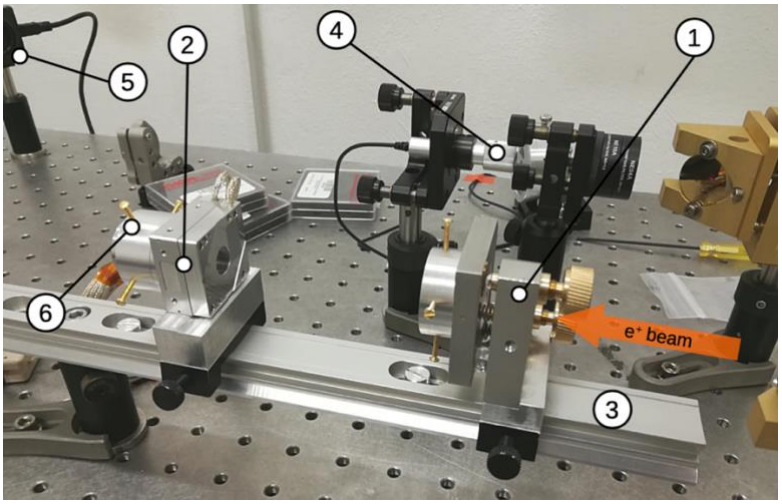

Figure 2.14: image of the rail with the two gratings, mounted on an optical table.

The alignment of the grating is a crucial part for the good success of the experiment. As shown in Figure 2.14, the system of the gratings is mounted on an optical table. The first grating holder (1) is a mirror mount, made of non-magnetic materials; the second grating is placed on a piezoelectric rotator (2), which is important for rotational alignment. The gratings are mounted on aluminum disks which can be moved on the x−y plane using the brass screws (6); this is used to center with a good precision the two gratings with the optical axis. The gratings are mounted on a support rail (3). The laser used for the rotational alignment (and also for the alignment with the optical axis) (4) is a Thorlabs, Inc.[31] CPS670F, 670 nm, 4.5 mW diode laser. Then, there are the two cameras (5), which are Thorlabs DCC1545M, equipped with a 1280 × 1024 CMOS sensor (pixel size is 5.2 μm); they are used for rotational alignment.

First of all, we present a method used for aligning the two gratings at the same height and with the laser beam.

This is done using a screw mounted on a collimator. The diameter of the screw is around 2.5 mm and is positioned so that the laser impinges into the tip. Then the support with the screw is put in the vicinity of the first grating (as in Figure 2.15). The height of the grating is then confronted with the screw and correct. The same is

done for the second grating. In this way, the alignment with the optical axis is assured.

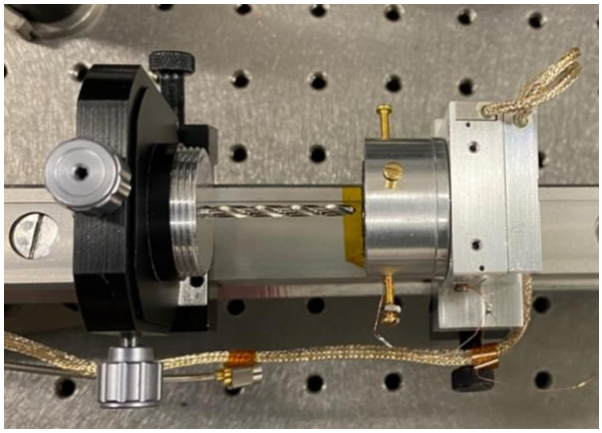

Figure 2.15: image of the screw used as a reference to align the gratings.

2.5.1. Longitudinal alignment

Longitudinal alignment is about setting the right distances between the components of the interferometer. First of all, we have the periodicity of the gratings; the values are given by the manufacturer:

$$d_1 = (1.2097 \pm 0.0003)\ \mu m \tag{2.3}$$

$$d_2 = (1.0047 \pm 0.0003)\ \mu m \tag{2.4}$$

$$\frac{d_1}{d_2} = 1.2040 \pm 0.0005 \tag{2.5}$$

Therefore:

$$d_3 = \frac{d_1 d_2}{d_1 - d_2} = (5.93 \pm 0.01)\ \mu m \tag{2.6}$$

Recalling eq.(2.1), we know that:

$$\overline{L_2} = \frac{\overline{L_1}}{\frac{\overline{d_1}}{d_2} - 1} \tag{2.7}$$

where $\overline{L_1}$ is the experimentally measured value and is affected by an uncertainty δL_1. We can estimate that the uncertainty of $\overline{L_2}$ results in:

$$\delta L_2 = \overline{L_2}\sqrt{\left(\frac{\delta L_1}{\overline{L_1}}\right)^2 + \left(\frac{\delta r}{r-1}\right)^2} \tag{2.8}$$

With $r = d_1/d_2$. Since $\overline{L_1}$ is in the order of 12 cm, $\delta L_1 \cong 0.1\ mm$ and the uncertainty δ_{L_2} is of the order of 1 – 2 mm. This value must be compared with the longitudinal extent of the interference fringes σ_{L_2}. The latter depends on beam coherence, so the degree of coherence of the beam should be increased to the point that $\sigma_{L_2} \geq \delta L_2$. This explains why we need to put at the end of the optics a mechanical collimator, as presented in Sec. 2.3. This is useful to improve the coherence of the beam to fulfill the condition presented previously.

To measure the various distances a system which moves along the interferometer rail is used. The position is read by a linear scale (Mitutoyo ABS AT715 series [32]) (Figure 2.16).

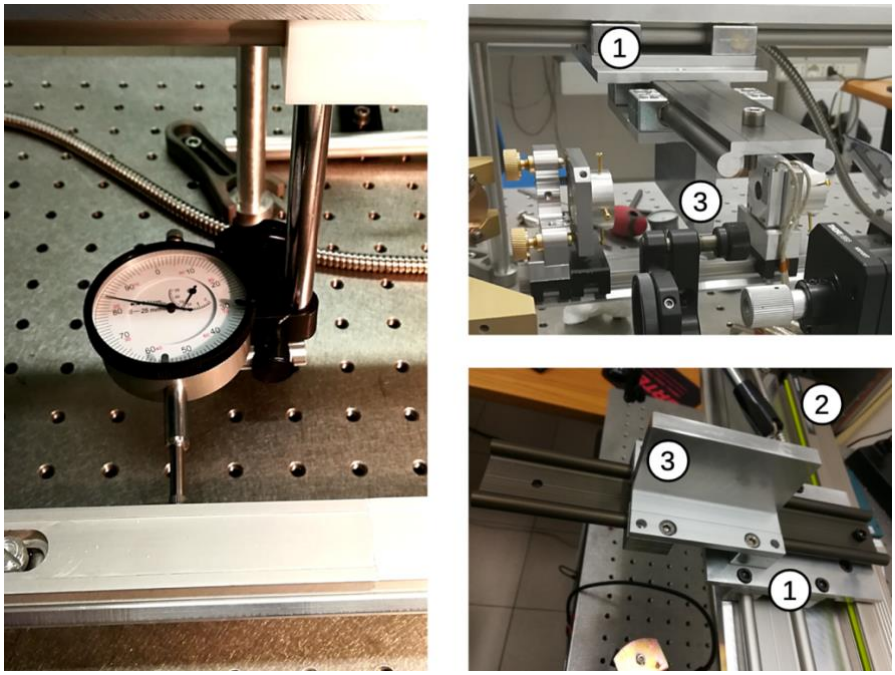

Figure 2.16: system used to measure the longitudinal distances. (1) and (3) show the two degrees of freedom of the system, (2) is the rail on which the system runs.

2.5.2. Rotational alignment

The rotational alignment of the two gratings is relevant in carrying out the experiment. Indeed, the two gratings should be parallel, in order to see an interference pattern. The approach adopted to align the gratings consists in rotating the second grating, mounted on a piezoelectric rotator. However, since no direct measurement of the alignment is possible, due to the low intensity of the positron beam, an indirect method is adopted. When a diffraction grating is illuminated by a plane wave, it produces a series of diffraction maxima, whose position is described by the following formula from geometrical optics:

$$\theta_n = \arcsin\left(n\frac{\lambda}{d} + sin\theta_i\right) \tag{2.9}$$

where d is the periodicity of the grating, θ_i the angle of the incident plane wave with respect to the normal and $\theta_n$the angle of the diffracted ray of order n. In our method we focus on the first maxima of diffracted light. Recalling to the fact that the first grating has a larger periodicity than the second grating, the first grating diffracts light at a smaller angle. This makes possible the existence of an intersection point between the two diffracted spots.

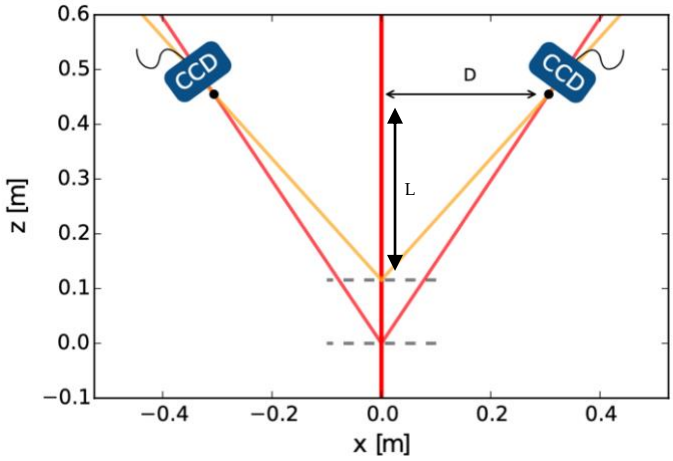

Figure 2.17: sketch of the principle for alignment. The dashed grey lines represent the two gratings. the black spots are the superposition of the two diffracted rays and should coincide with the cameras.

The intersection points are marked by black dots and are located at a distance $D \approx 30\ cm$ from the optical axis and $L \approx 30\ cm$ downstream the second grating (Figure 2.17). The cameras are placed at these distances and a filter is positioned before the cameras in order to decrease the intensity of the first grating spot and make the two spot intensities comparable. Obviously, the ideal rotational alignment condition is met when the two pairs of spots (two on the left side and two on the right side) coincide at the cameras in the same plane perpendicular to the gratings (Figure 2.20).

If one of the gratings is rotated by an angle φ along the optical axis, the diffracted laser spots move on a circle of radius D on the plane orthogonal to the optical axis which contains the points of intersection (Figure 2.18).

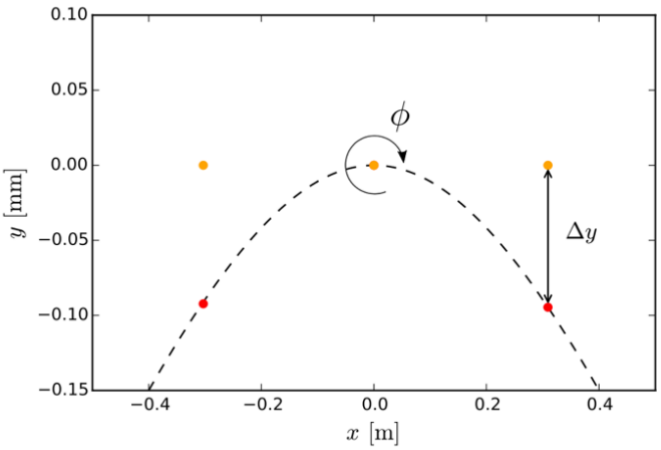

Figure 2.18: representation of the effect of the relative rotation of one grating.

If the laser spots on both sides are superimposed with an uncertainty δx, the error on the alignment angle is estimated as:

$$\sigma_\phi \approx \frac{\delta x}{D} \tag{2.10}$$

Now there is description of a protocol, which is able to achieve few tens of μrad of accuracy in rotational alignment. As we see in Figure 2.19, the laser spot on the two cameras (bottom-left) are elliptical. An algorithm [39] (written in Python) is employed to make the Gaussian fit for both the directions. Now, rotating the second grating the superposition of the two spots is searched. When this condition is achieved, a better alignment is researched. This is achieved when the smallest full width at half maximum (FWHM) is obtained. Once find this condition, the rotation is fixed.

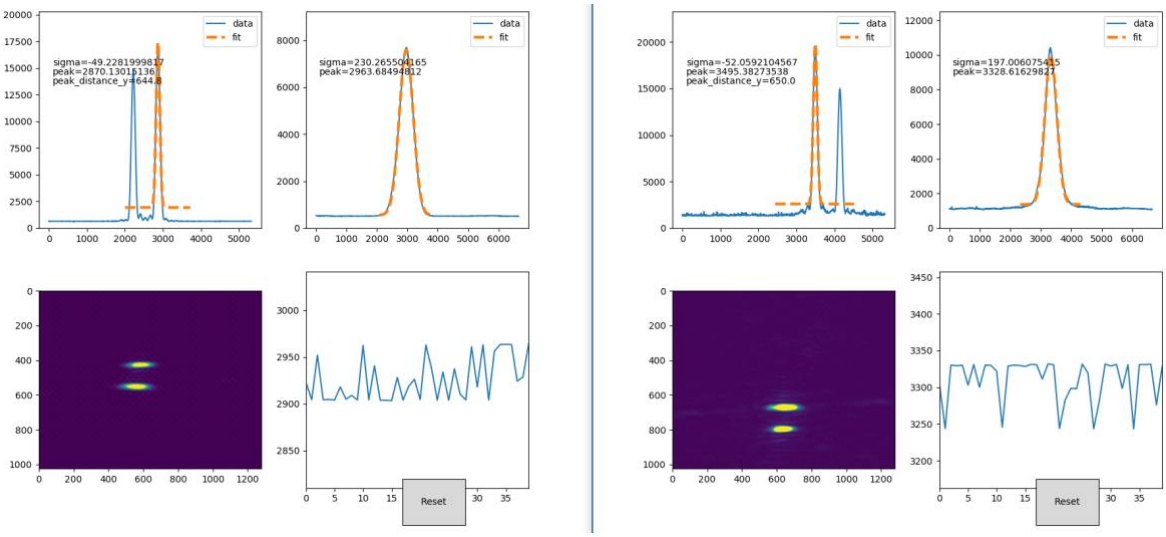

Figure 2.19: bad rotational alignment, with the two spots separated in both cameras.

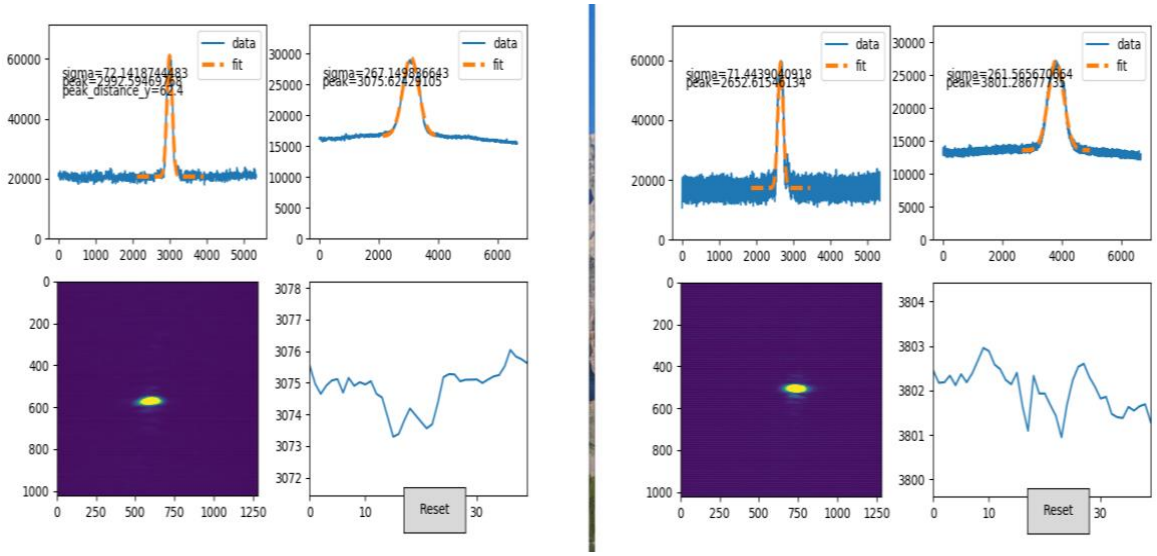

Figure 2.20: good rotational alignment, with optimal superposition of the spots. It is optimized the FWHM of the sum of the spots.

Since this rotational alignment is done in the optical table, the system should be then placed inside the chamber. To make the system stable, which means keeping the correct alignment, the piezoelectric rotator should be kept ON also when the gratings are inside the chamber.

2.6. Microwave modulus

The plan is to supplement the apparatus by a cavity located after the second grating, in which a standing microwave field is generated. In a "classical" language the single positron crossing the second grating will interact with photons in the microwave field. It is this interaction that we plan to study with the QUPLAS *Quantum revival* experiment.

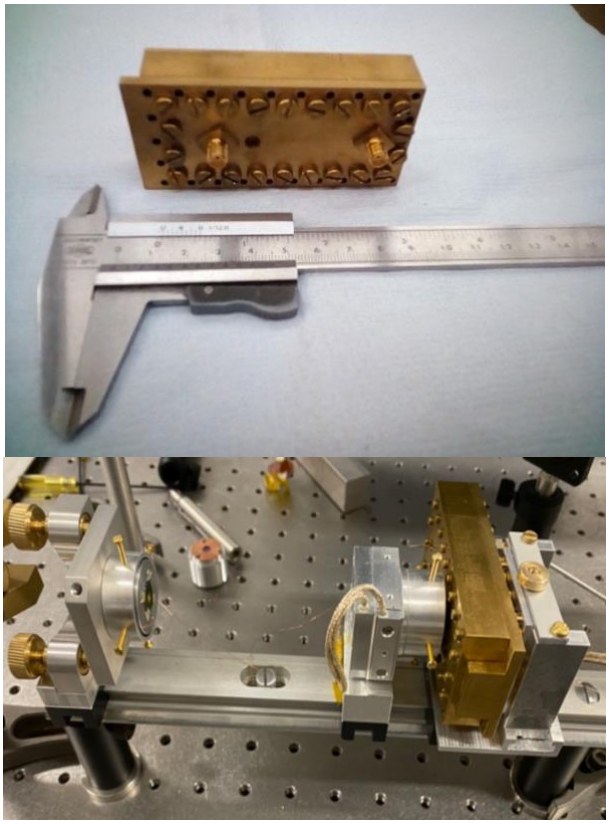

Figure 2.21: image of the microwave cavity alone (above) and mounted after the second grating on the optical table (below).

The electromagnetic field is produced by a microwave cavity schematized in Figure 2.21. It is made by M. Leone at the L-NESS Laboratory and designed by A. Simonetto and G. Gittini at the Istituto di Fisica del Plasma del CNR in Milano, where several tests have been made.

The cavity is a special type of resonator, consisting in a structure made of brass, which has a very-low-magnetic influence on the positron beam. It confines electromagnetic field in the spectral region of the microwaves. The microwaves bounce back and forth between the wall of the cavity and at the cavity's resonant frequency they reenforce to form standing waves. The cavity is characterized by extremely low losses at the resonance frequency, resulting in a moderate quality factor Q.

Positrons enter in a node, interact with the standing microwave field and exit. The beam duct, located at a node, is close to the center (1 in Figure 2.22). The conductor exiting the cavity is on the left, highlighted in magenta (2 in Figure 2.22). A power monitor port is placed at the field maximum, on the right (3 in Figure 2.22). The field is externally tunable by changing the microwave power. The power is selected using attenuators. Changing the attenuation, it is possible to repeat the experiment with

different intensities of the electric field, following the scheme in Figure 2.23. The reduced-height waveguide between the input port (magenta) and the beam duct is used to increase the quality factor Q.

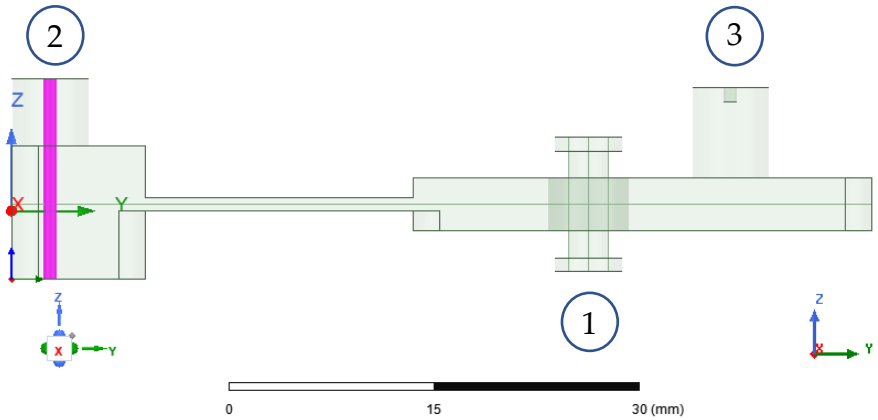

Figure 2.22: sketch of the microwave cavity.

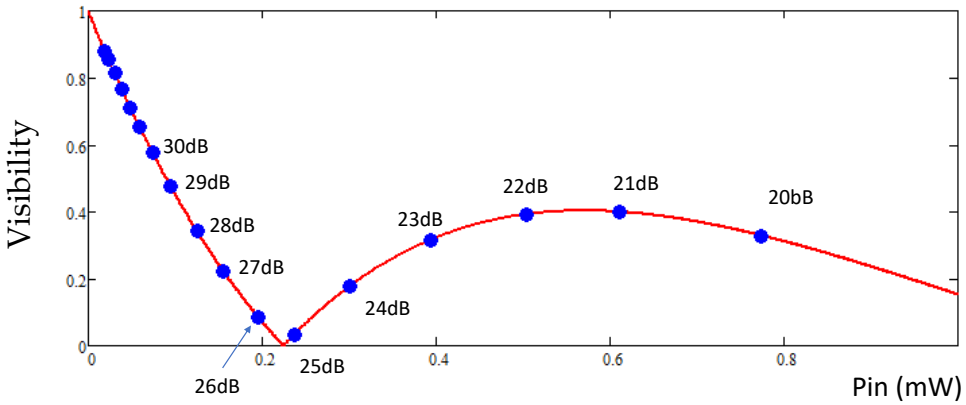

Figure 2.23: sketch of the different attenuations to obtain different values of power in the cavity.

Figure 2.24 shows the cavity response function. It illustrates the position of the resonance peak, that corresponds to 9.85 GHz.

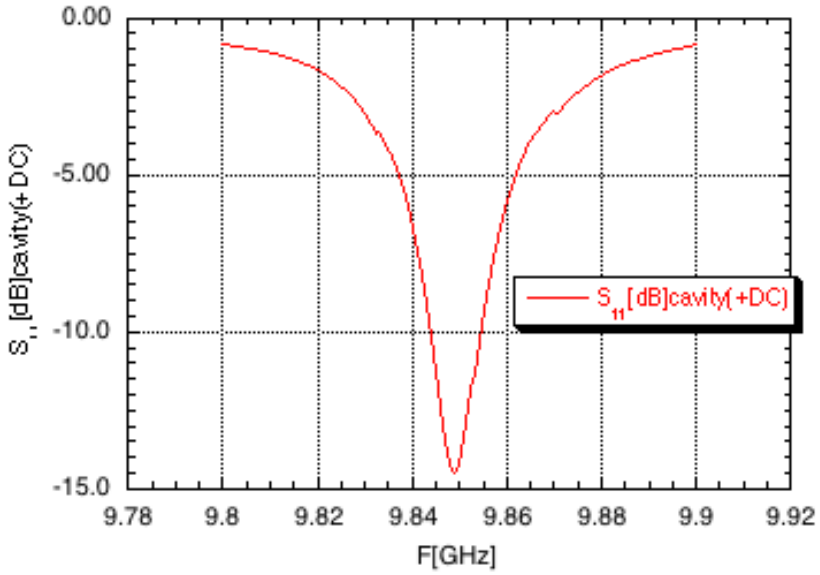

Figure 2.24: reflected power of the cavity at input port around resonance frequency.

Recalling Sec. 1.5, it is important to know the shape of the electric field. Indeed, it is the field that the positron will "see" entering the cavity. The components are shown in Figure 2.25.

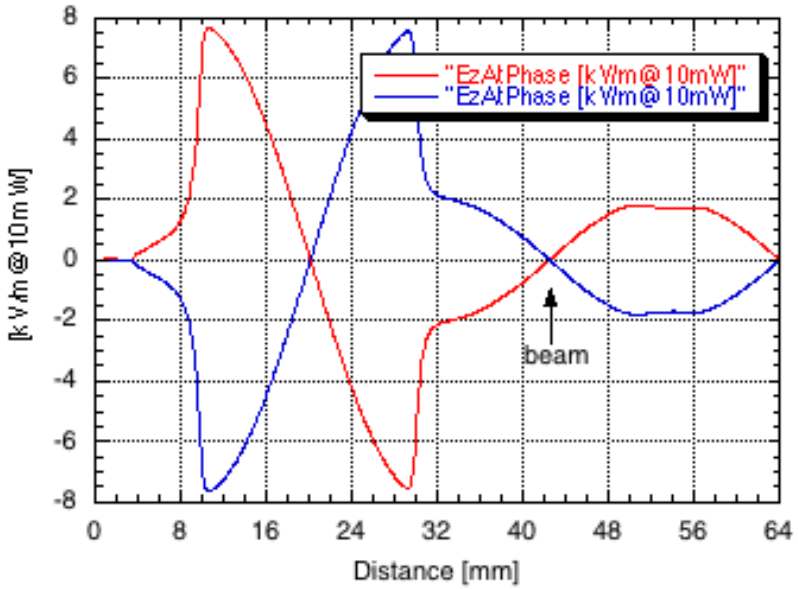

Figure 2.25: component of the electric field along the cavity.

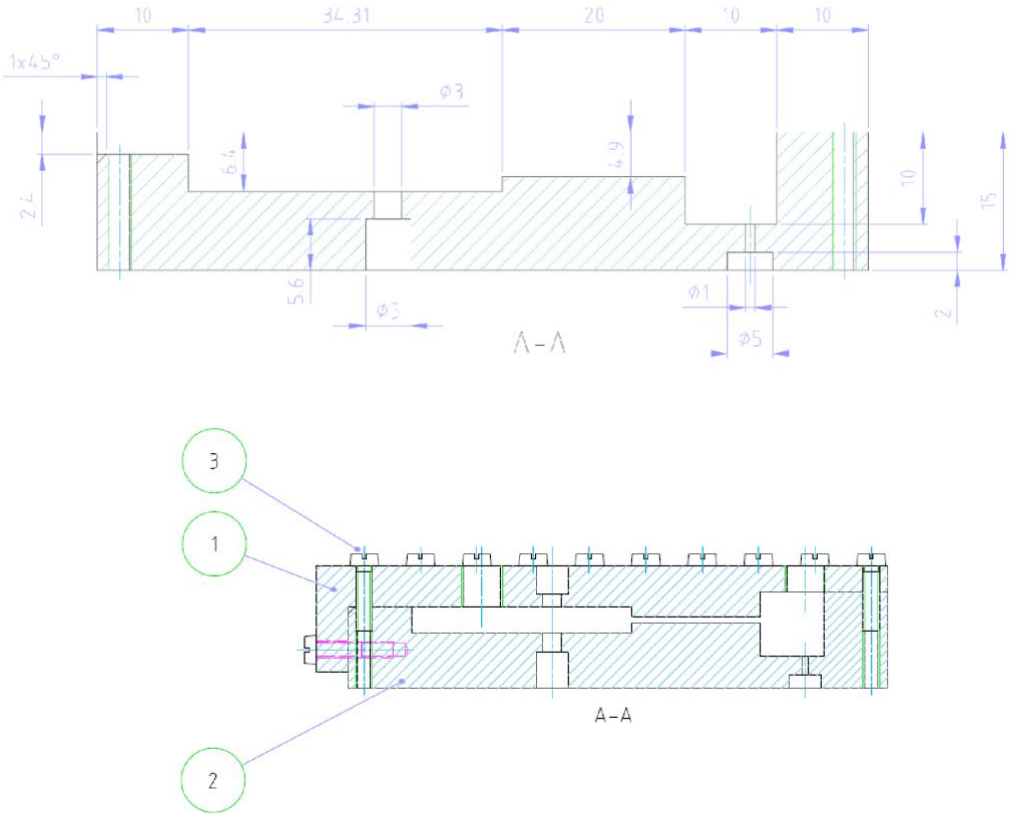

Figure 2.26: some sketches of the microwave cavity.

2.7. Detectors

Detectors are used during the experiment and during the preparation of the experiment itself and have different goals. In particular, they are used for revealing the interference pattern (emulsion detector), for monitoring the number of positrons (HPGe) and for a real-time monitoring of the beam (MCP).

2.7.1. Emulsion detector

In the previous sections, when describing the Talbot-Lau interferometer, it was presented that at the detector the periodicity of the fringes is expected to be around 6 μm. Therefore, a resolution better than 1 μm is required to resolve the periodicity. Nuclear emulsions have a sub-micrometric resolution, which makes them good options for positron interferometric studies [34].

Figure 2.27: image of the glass support used to deposit the emulsion

Nuclear emulsions are composed by silver bromide microcrystals with an average diameter of 40 nm, embedded in a gelatin matrix. The kinetic energy released by the positron is transferred to the silver bromide microcrystals, resulting in the creation of a silver grain in the order of 1 μm, visible through an optical microscope. The emulsion is characterized by a low background of thermally induced grains, around $1-2\ grains/1000\ \mu m^3$ [33, 34].

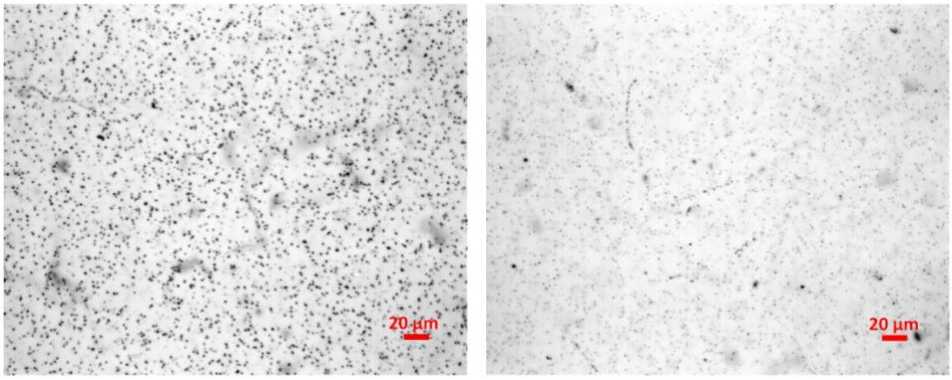

Figure 2.28: image of the center of the spot (left) and of a region not exposed (right) [34].

The gel is poured on a support made of glass, which ensures the necessary stability for the detection of patterns. Glycerin is also added to the gel (1.5% of concentration) to allow operation in vacuum.

Absorption of positrons by the emulsion protective layer must to be taken into account, and this was performed by adapting a semi-empirical model [35, 36] based on the parametrization of Monte Carlo simulations. The total rate detected on the emulsion n_{emu} is related to the incoming rate n_0:

$$n_{emu}(E) = n_0 T(E) \epsilon_{emu}(E) \tag{2.11}$$

where $T(E)$ is the transmission percentage of the protective layer and ϵ_{emu} is the intrinsic emulsion efficiency.

The new generation of nuclear emulsions are produced by the Giovanni De Lellis' group at the Gran Sasso Laboratory. After each exposure the emulsions are digitalized in this scanning facility.

The silver grains are reconstructed as clusters by a specific algorithm which assigns them their corresponding (x, y, z) coordinates both in a coordinate system local to the view, and in a global reference frame that considers the stage position [38]. Then, data are subdivided into regions called views ($370\,x\,240\,\mu m^2$). Each view is independently analyzed, searching for a periodicity, maximizing the so-called Rayleigh test function:

$$R(\alpha, d_3) = \left| \frac{1}{n} \sum_{j=1}^{n} \exp\left(\frac{2\pi i X_j(\alpha)}{d_3} \right) \right| \tag{2.12}$$

The analysis of the emulsion data needs to consider the rotational angle α between the microscope reference frame and the laboratory. Therefore, the periodic signal is expected in a linear combination of x and y, for instance $t = -x\,sin\alpha + y\,cos\alpha$, with α to be determined. X_j represents the coordinate of the j-th grain. A Gaussian fit is used to find the optimal period and angle. Once d_3^* and α^* are found, a histogram of $X_j(\alpha^*)$ and d_3^* is constructed. The contrast is obtained by fitting the histogram with a sinusoidal function [37]. The measured contrast follows the usual definition:

$$C = \frac{I_{max} - I_{min}}{I_{max} + I_{min}} \tag{2.13}$$

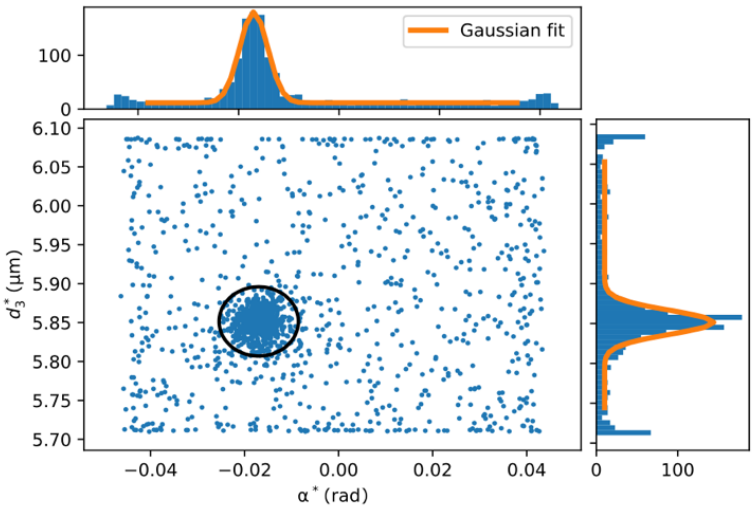

Figure 2.29: optimal angle and period found via Rayleigh test [2].

Positrons at 14 keV can penetrate few micrometers in the volume of the emulsion from the surface before the annihilation event takes place. As a consequence, a signal of the developed grains near the surface is the signature of positron impinging and releasing energy to the grains (Figure 2.30).

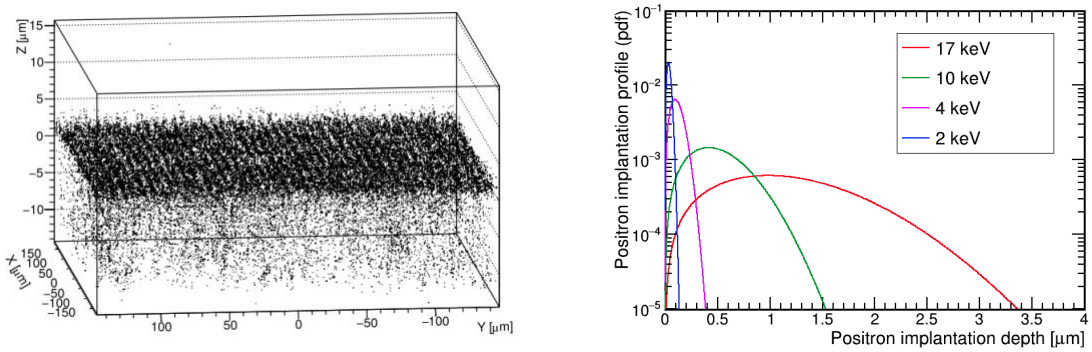

Figure 2.30: left: distribution of a pattern on the silver grains. The sharp peak near the surface is the signature of positron annihilation grains. Right: positron implantation profile [33].

2.7.1.1. Background noise

The main sources of background noise in the interferometric measurement are:

- contribution of positrons transmitted through the grating bars,
- intrinsic emulsion noise.

The first refers to those positrons which are transmitted from the closed portion of the gratings. Even though the gratings are thick, the positrons have high energy, therefore, they penetrate the bars. The ones transmitted produce a uniformly distributed pattern (almost gaussian on a large scale) superimposed with the interferometric signal [38]. However, a geometrical argument can prove that this source of noise is negligible in terms of the periodicity. Indeed, if positrons are propagated as ballistic particles from the plane of the second grating with a Gaussian angular distribution with $\sigma_\beta = 0.57\, rad$, they are found to be distributed on the detector plane with $FWHM_{noise} \approx 0.8\, m$. On the other hand, the typical size of the detected positron spot in the interferometric measurements we performed is $FWHM_{signal} \approx 6.5\, mm$ [39]. Therefore, in terms of signal surface density, the contribution of this source of noise is suppressed by a factor proportional to $(FWHM_{noise}/FWHM_{signal}) \cdot 2 \approx 10^4$.

The second background contribution is the intrinsic emulsion noise, which is energy independent and is due to thermally induced grains that appear in the emulsion films. This kind of noise is different for different emulsion batches and is mainly related to the storage and transportation of the emulsion and time spent in vacuum.

The thermal component is the dominant one, with respect to other sources, like Compton electron mainly from annihilation events or cosmic rays. This thermal noise can be considered uniformly distributed and is not directly proportional to

the exposure time [39]. Therefore, increasing the exposure time will results in an increased signal to noise ratio.

2.7.1.2. Periodicity test

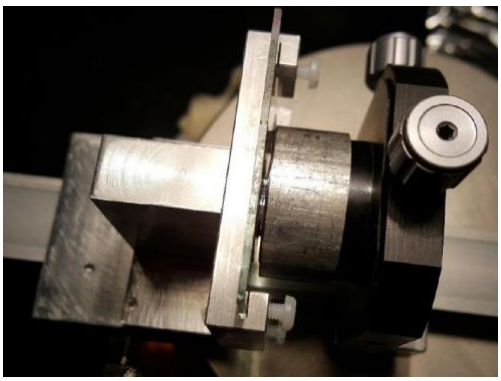

Figure 2.31: image of the grating putted (almost) in contact with the emulsion.

In order to assess the performance of the emulsion to distinguish the periodicity of a pattern, an experimental test was performed. It consisted in placing a grating of periodicity of 7 μm in close contact with the emulsion surface (Figure 2.31). In this way it worked as a mask for the positrons, which came to the emulsion producing the periodic pattern of the grating. In other words, they projected the periodicity of the gratings on the emulsion.

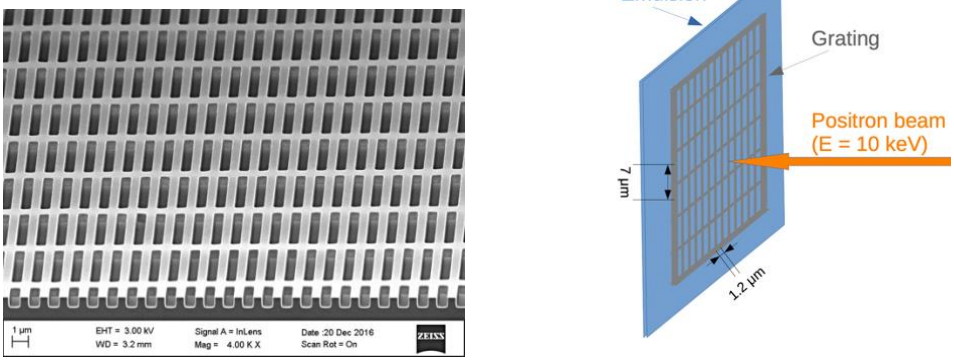

Figure 2.32: image and sketch of the grating with periodicities: 1.2 μm along the horizontal direction and 7 μm along the vertical direction.

The grating used was produced by LumArray Inc. [37], specifically for QUPLAS-0. The transmissive region is a free-standing silicon nitride (SiN) membrane, approximately 700 nm thick, coated on both sides with a 10 nm thick gold layer to prevent charge build-up. The free-standing area has a surface of $3 \times 3\, mm^2$, and is patterned with a system of rectangular apertures. Slits have a periodicity $d1 = (1.2097 \pm 0.0003)\, \mu m$ and an approximately 50% open fraction run along the

horizontal direction. In the orthogonal direction, the structure has a period $d2 = (7.00 \pm 0.05)\ \mu m$ and an open fraction of (79 ± 3)% (Figure 2.32). The goal of this test was to observe the periodicity of 7 μm.

The grating was mounted on a grating holder that was aligned and placed almost in contact with the emulsion. The estimated distance between the two was $\Delta X \sim 200\ \mu m$ (Figure 2.33).

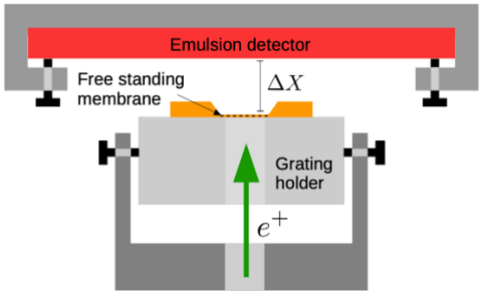

Figure 2.33: sketch of the distance grating-emulsion.

To conduct this measurement the specifications listed in Table 2.3 were chosen.

E (keV)	$FWHM$ (mm)	V_F (kV)	*exposure time* (*hours*)	*number of positron per second* (e^+/s)
10	~3	5.615	4.1	$\sim 2 \cdot 10^4$

Table 2.3: characteristics of the periodicity test on emulsions.

The kinetic energy of positron was fixed at 10keV. This energy was chosen to reduce the positron transmission with respect to the case of 14keV. The focalization voltage was chosen so that the beam resulted focalized in the position of the grating/emulsion, so in the center of the chamber. It corresponded to 5.615 kV.

The 7 μm pattern was detected on the three different emulsions, under different conditions of vacuum:

- Emulsion 1: $p = 7 \cdot 10^{-7}$mbar.
- Emulsion 2: $p = 6 \cdot 10^{-7}$mbar.
- Emulsion 3: $p = 1 \cdot 10^{-6}$mbar (not optimal condition of vacuum).

The fact that the three tests were performed with different levels of vacuum results to be very interesting; indeed, it could give us an idea of the impact of a non-optimal vacuum on the contrast, so on the pattern measurement.

2.7.1.3. Results of the exposures

Emulsion 1

From Figure 2.34, the signal after correction (bottom-right) shows a clear periodic pattern, visible also at naked eye. The contrast (top-right) is around 30%. It is possible to conclude that the periodic structure is well resolved in this first case.

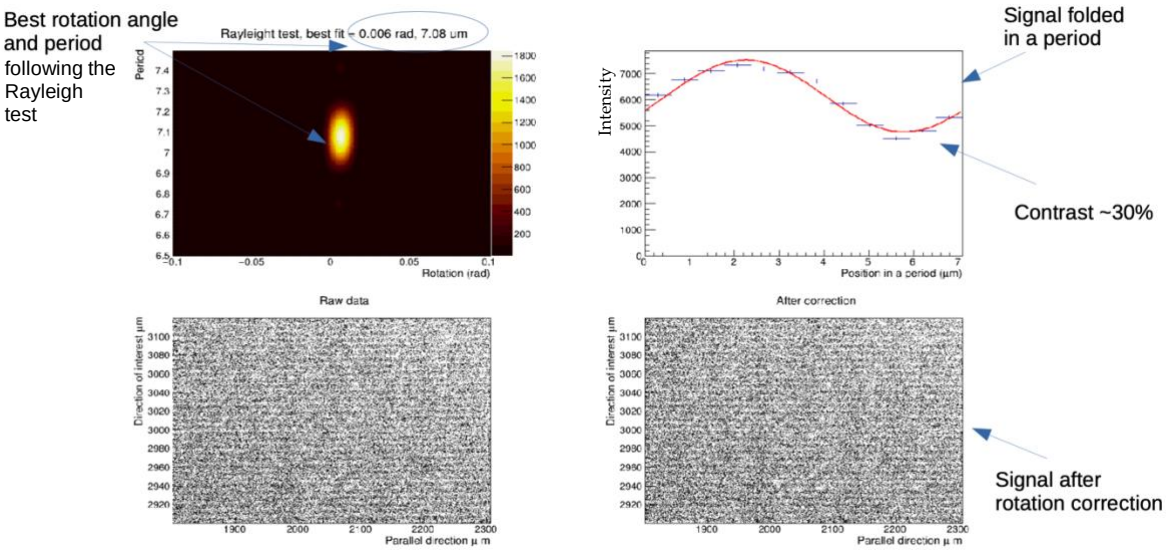

Figure 2.34: results of the emulsion 1.

Emulsion 2

In the second emulsion, it is noticeable a well resolved periodicity and a contrast around 30%, as in the case of the first emulsion. The two, indeed, are characterized by similar condition of vacuum.

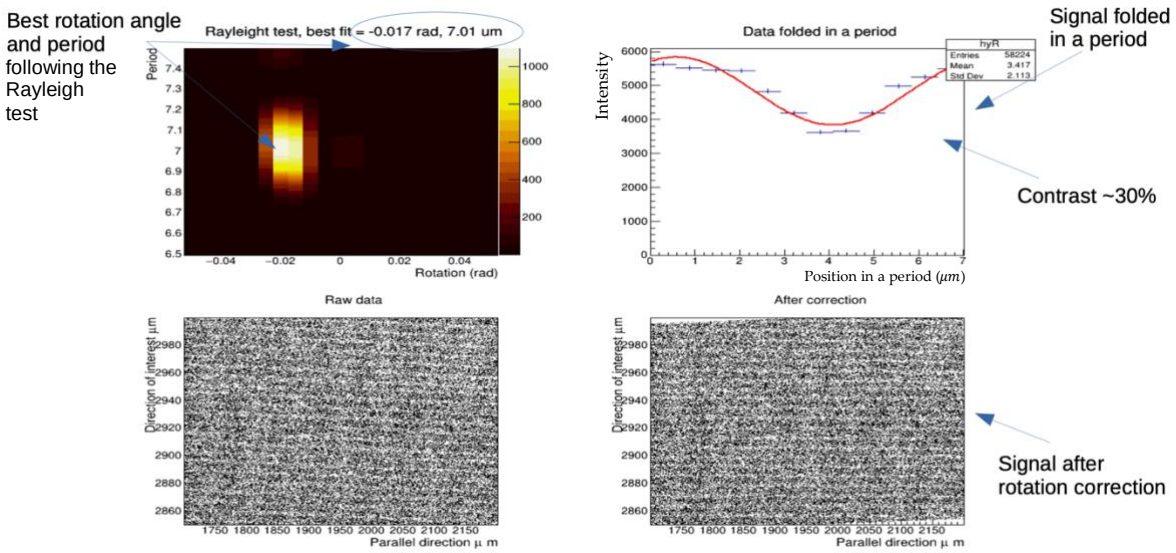

Figure 2.35: results of the emulsion 2.

Emulsion 3

The third emulsion was the worst vacuum case (higher pressure in the chamber). In this case, the contrast is decreased with respect to the other two emulsions and is around 25%. However, it is important to notice that also in this case the periodicity was resolved.

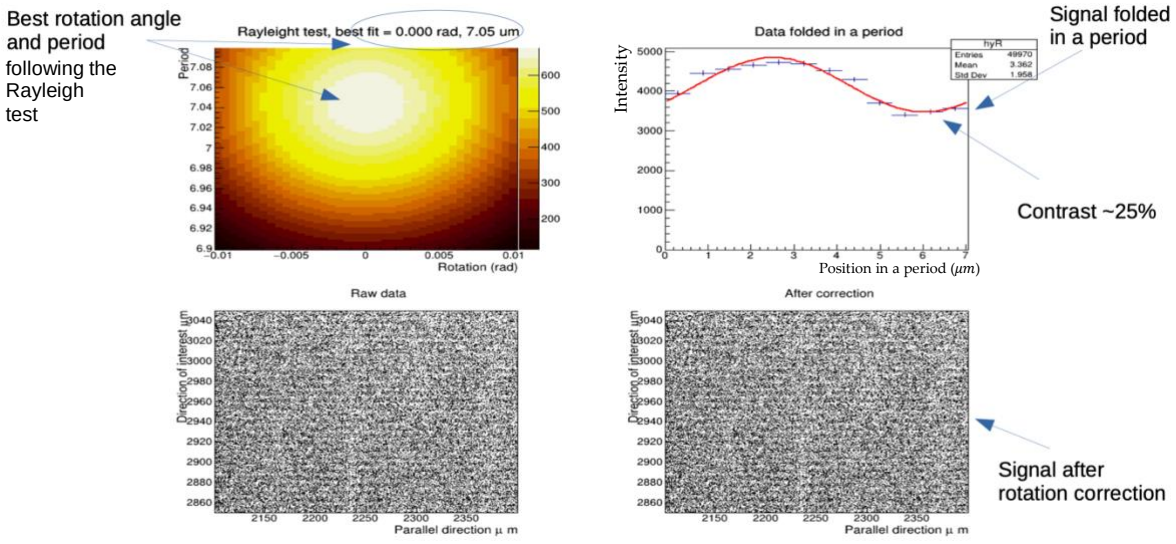

Figure 2.36: results of the emulsion 3.

It is possible to conclude that in all the cases the periodicity is well resolved and the condition of the vacuum does not affect too much the capability of resolving the periodicity, but results in a decreased contrast.

2.7.2. Germanium detector

One of the detectors used in the experiment is the Hyper Pure Germanium detector (HPGe). This is used to reveal the annihilation of positrons and is used primarily to quantify the positrons. Indeed, a positron annihilates with an electron, releasing two gamma rays at 511keV, in according to:

$$e^+ + e^- \rightarrow 2\gamma_{511keV} \tag{2.14}$$

A way to reveal the presence of a positron is to reveal the number of gamma rays at 511keV.

The physical principle is that the gamma ray to be revealed creates an electron-hole pair in the semiconductor material [40]. The high resolution of this kind of detector is due to the small energy needed to create an electron-hole pair, thanks to the small energy gap (typical of semiconductor). Applying an electric field, the electron and the hole move in the opposite direction creating an electric signal.

To do this a p-n junction must be created. In the region of contact, it is created a depletion region: a region that lacks of carriers, which is the active region. Since gamma rays are very penetrating, this kind of detector needs a consistent width of the depletion region, in the order of some cm. It is possible to demonstrate that the depletion width is inversely proportional to the square root of the concentration of impurity in the semiconductor [40]. It is clear that, in order to have a detector suitable for high penetrating radiation, a high purity semiconductor is needed. In HPGe detectors the number of defects is lower than $10^{10} atoms/cm^3$, with respect to the $10^{22}\ atoms/cm^3$ of germanium atoms.

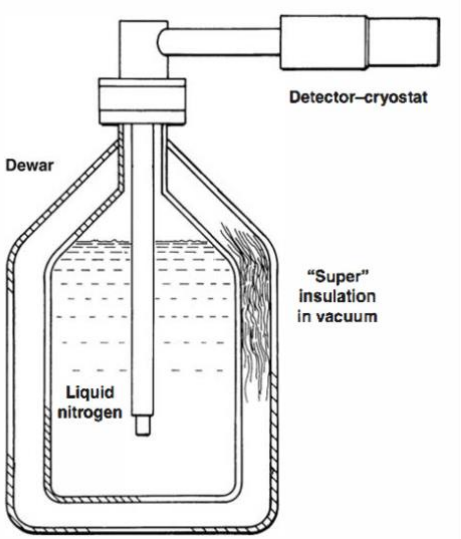

Figure 2.37: sketch of a HPGe detector.

Another important aspect is the influence of temperature; due to the small energy gap of germanium, it would be impossible to operate at room temperature. Indeed, the great majority of the electron-hole pair would be generated by thermal effect. Therefore, this kind of detector works at 77K, being taken in contact with liquid nitrogen, as schematized in Figure 2.37.

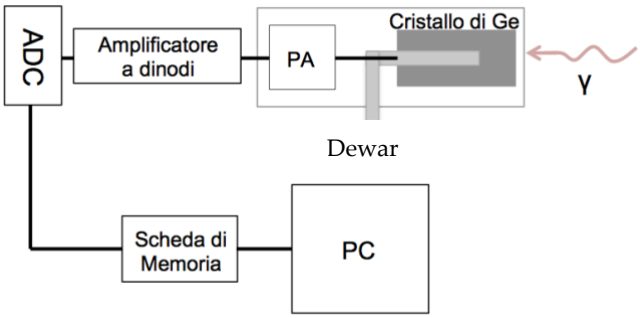

Figure 2.38: sketch of the signal reading circuit.

The signal coming from the detector, corresponding to an event of revelation, must be pre-amplified by a preamplifier (PA in Figure 2.38), contained in the detector itself. Then an ADC converter is used to read the signal using a PC. An example of the revelation spectrum is presented in Figure 2.39, where the greatest peak represents the 511keV peak.

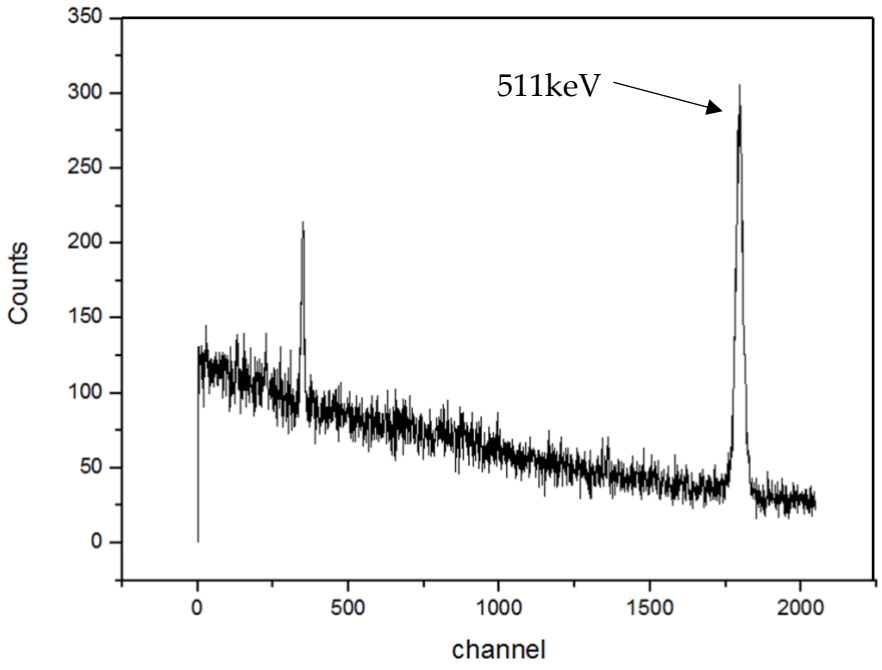

Figure 2.39: example of a graph obtained using a HPGe detector.

2.7.3. MCP

The positron beam was characterized using a microchannel plate (MCP). The method used offers the possibility to get information about the dimension of the spot and to quantify the particles per unit time interacting with the MCP. Even if the spatial resolution of other types of detectors, like emulsions, is better, the MCP has the advantage of monitoring the beam in real time.

The system consists of an MCP, a phosphor screen and a CCD camera [41]. The MCP consists of a 2-stage v-like stack of microchannel plates made of lead glass coated with a nickel-based alloy (Inconel) [41]. The effective size of the MCP is 27 mm in diameter, while channels have a diameter of 12 μm; they are tilted at an angle of 8° with respect to the longitudinal axis of the MCP. The open area ratio of this MCP is 60%. By applying a positive voltage difference between the entrance and the exit of the channels (set in this work at +1.5 kV), an interacting particle produces an electron shower via secondary emission.

The MCP is coupled to a P43 type phosphor screen with an effective size of 24 mm in diameter, at a distance of 1 mm downstream of the MCP. This phosphor features a peak emission wavelength of 550 nm and a decay time of 1.5 ms at 10% of the light intensity [41]. Thanks to a potential of a few kV (set to +2.6 kV) between the exit of the MCP and the phosphor, the electron shower is accelerated to hit the phosphor

grains. Here, thanks to the fluorescence process, the electron avalanche is converted into photons, which can be observed by means of a CCD camera. The beam, the MCP and the phosphor screen operate in vacuum at pressures between 10^{-6} and 10^{-8} mbar, while the digital camera is in air. The end of the chamber is constituted by a glass, which allows the direct observation of the phosphor screen.

To summarize, positrons coming from the beam interact with the MCP and appear on the phosphor screen as bright spots in an image that is digitized using a CCD camera. Then, through the use on an algorithm implemented in MatLab®, it is possible to do a Gaussian fit of the beam and extract the dimension of the spot and the total number of positrons.

When it is necessary to characterize the intensity of a continuous beam, a statistically significant number of particles is required (10^4–10^6 particles). However, it is not possible to exclude the possibility of overlapping when an image contains more than one spot. This depends on several parameters: the number of single spots, their size and the size of the beam. Overlapping often makes it impossible to distinguish between different signal sources, so reducing detection efficiency; this means that the observed number of spots for a given frame may be less than the actual number of positrons. A numerical simulation has been performed [41] in order to calculate the overlap probability. Results of these analysis are reported in Figure 2.40.

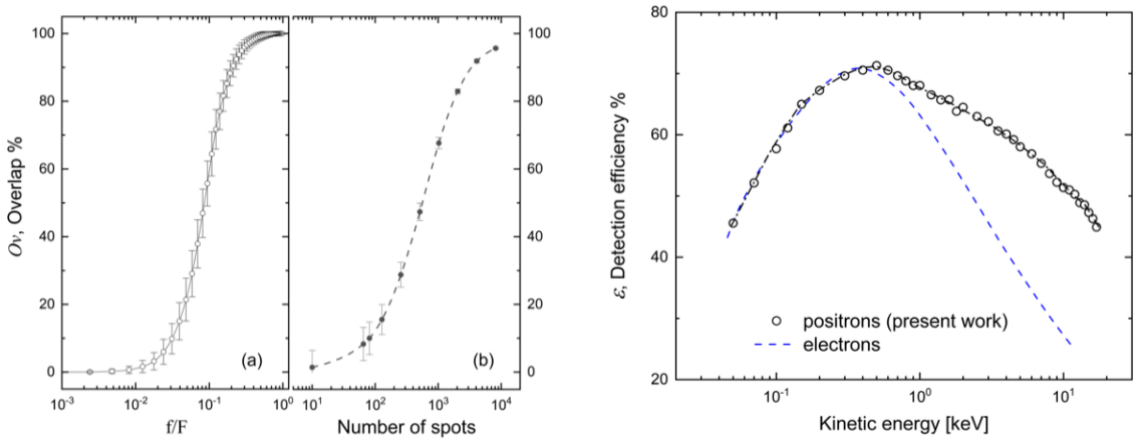

Figure 2.40: overlap probability (left) and detection efficiency (right) [41].

One strategy to reduce the overlap probability is to acquire many short-lived frames (with limited number of spots) and merge them later via software. The necessary total exposure time depends on the beam intensity and on the spot size. Taking into account the characteristics of the present setup, we have typically set 1 ms as the frame exposure time.

In Figure 2.41 we see an example of a frame. Each frame can be seen as a matrix of pixels, which take a value between 0 (no light signal or noise) and $2^{14} - 1$ (saturation) on a scale of intensity. Through the MatLab® algorithm a digital histogram is constructed for every frame, as in Figure 2.41. It is clear that every spot follows a nearly Gaussian distribution. Then, all the matrices of each frame are superimposed to recreate the overall beam intensity profile. Using a MatLab® script it is possible to do a Gaussian fit, obtaining the total number of spots and the dimension (FWHM along x and along y) of the Gaussian beam. This method was really useful during the characterization and specially the optimization of the beam (Sec. 3.1).

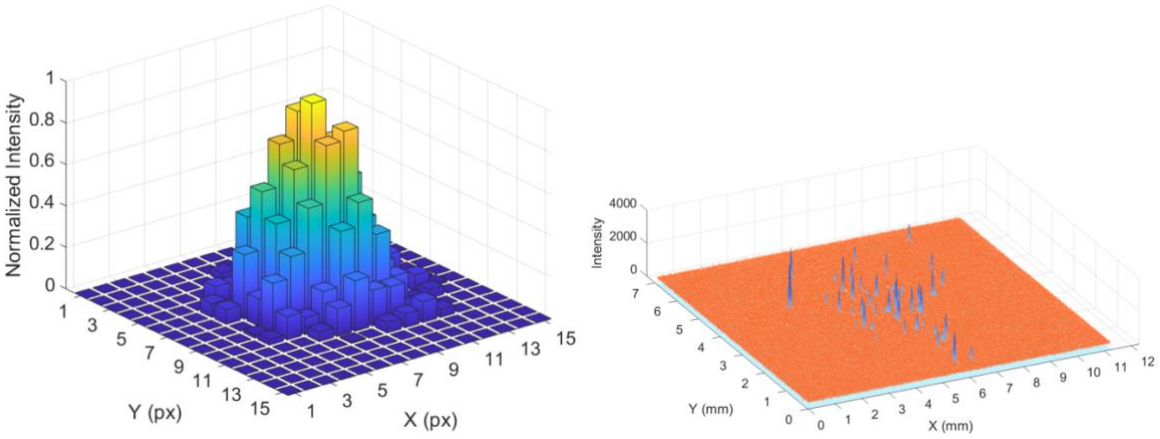

Figure 2.41: histogram of a single spot (left) and Gaussian fit of each spot for a frame (right) [41].

The average measured resolution of the single spot is 60 ± 2 μm [41]. The secondary electron shower that reaches the phosphor screen has two velocity components, in the longitudinal and transverse direction. The longitudinal component is due to the potential difference between the MCP and the phosphor screen (2.6 kV). The transverse one corresponds to the energy with which the secondary emission from the tubes takes place, that is an energy distribution up to 100 eV [42]. To a first approximation, the overall shower trajectory between the MCP and the phosphor is represented by a cone. The emission angle of electrons can therefore be calculated as $\theta = arctan\left(\frac{v_y}{v_x}\right) = 1.5$. Considering the distance L_2 = 1 mm between the MCP and the phosphor screen, the electrons hit the phosphor within a circular region with a diameter of 50 μm. On the other hand, the indetermination of the position of the arrival point of each positron is given by the channel diameter (12 μm). This is why the MCP is a good instrument to monitor the beam, but not to observe the periodicity; it has not the resolution requirements to see the interference pattern.

3 Optimization of the beam

In this chapter, the characterization of the beam is presented, which means the measurement of the dimension of the spot and of the number of positrons per second; this is performed in different positions: in the middle of the chamber (1), where the first grating is expected to be and at the end of the interferometer (2), where the emulsion detector is expected to be (Figure 3.1).

Another important aspect is the optimization of the beam, which means the correction of the potentials applied to the optics in order to obtain a symmetric beam, suitable for the experiment. Of particular importance is the understanding of how the dimension of the spot and the number of positrons change upon changing the focalization potential and the corresponding choice of the best configuration.

The impact of the presence of a collimator at the end of the optics, fundamental element in the interferometry in Talbot-Lau configuration, is also investigated.

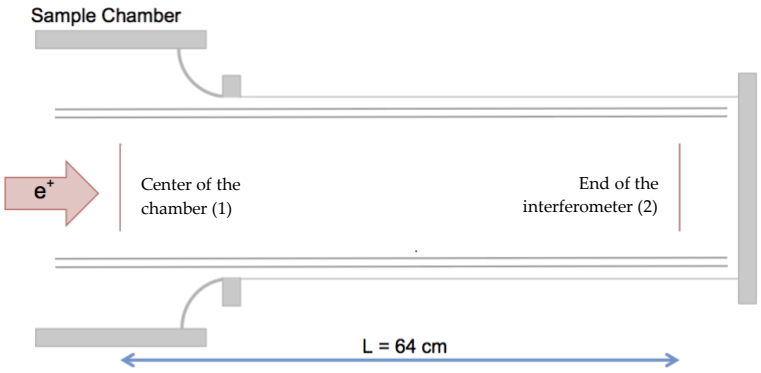

Figure 3.1: sketch of the two positions of characterization.

3.1. Dimension of the spot

The dimension of the beam is a crucial parameter in the experiment of interferometry. It is important to monitor the dimension of the beam, because it is preferrable to have a beam which is collimated, populated and with a small divergence between positions 1 and 2.

The gratings have dimensions of 3 *mm* x 3 *mm*; as a consequence, the beam (treated as gaussian) should be in the order of 2 *mm* in term of FWHM (at least around position 1).

The characterization of the beam dimension was done using the MCP (Sec. 2.7.3). This allowed a real time monitoring. 400 frames of 1 ms of exposure time were acquired for the analysis.

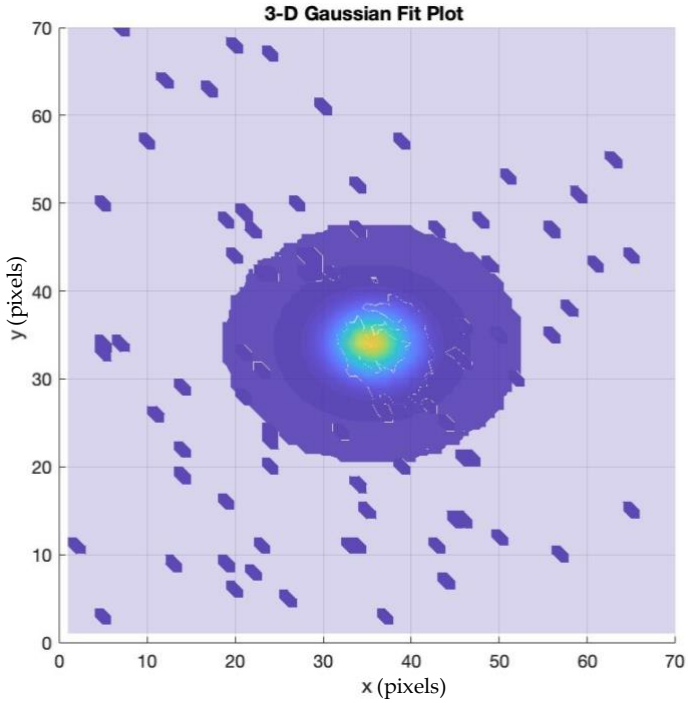

Figure 3.2: example of a Gaussian fit plot.

The first step was to characterize the starting condition of the positron beam in the middle of the chamber (position of the first grating). The measurement was performed at the beginning of the work. The positron energy used for this first characterization was 10 keV. This is the energy used during the periodicity test, explained in Sec. 2.7.1.2). The results are schematized in Table 3.1.

V_F (kV)	$FWHM_x$ (mm)	$FWHM_y$ (mm)	$number\ of\ positron\ (e^+/s)$
5.165	4.4	2.1	$\sim 5 \cdot 10^4$
5.8	2.8	1.8	$\sim 5 \cdot 10^4$

Table 3.1: characteristics of the beam.

It is clear that the spot resulted to be asymmetric. In particular, it was elongated along the x-axis. This could have been due to a non-perfect bending of the beam at the bender. This suggested that this parameter could be modified, to improve the geometrical quality of the beam.

The protocol adopted consisted in changing by few volts the values of some strategical tubes in the part of the electrostatic optics. However, for these corrections, the positron energy of reference was used, which is 14 keV (the one that will be used for the interferometric experiment). The MCP allowed to monitor the symmetry of the beam in real time; the MatLab® code allowed to have information (almost real time) about the FWHM in x and y and also to have an estimation of the number of positrons.

During the procedure it resulted evident that the tube before the bender and the bender itself were crucial for the quality of the beam. Indeed, how the positrons "make the curve" resulted important in term of symmetry and dimension along x. Other important parts were the deflection plates of tubes 5 and 7 which allowed to correct the position of the beam and its symmetry.

After some operations, the conditions schematized in Table 3.2 were found.

V_F (kV)	$FWHM_x$ (mm)	$FWHM_y$ (mm)	$number\ of\ positron\ (e^+/s)$
9	1.78	1.60	$\sim 10^4$

Table 3.2: characteristics of the beam after some manipulations.

The spot was really small and quite symmetric. The number of positrons remained quite similar after this optimization.

The next step was to mount the collimator. This was important to give the beam a better coherence. However, since it is a mechanical obstacle for the positrons, its presence may cause a modification of the characteristics of the beam. These must be investigated.

3.2. Effect of collimation

The collimator is a tube of aluminum of length $L = 10\ cm$, with an aperture of diameter $2r = 2\ mm$. Therefore, only the positrons inside this aperture can pass and reach the MCP, creating a bright spot (which is revealed). The others annihilate in the metal of the collimator. The characteristics of the beam after the mounting of the collimator are summarized in Table 3.3.

V_F (kV)	$FWHM_x$ (mm)	$FWHM_y$ (mm)	$number\ of\ positron\ (e^+/s)$
9	1.22	0.90	$\sim 10^3$

Table 3.3: characteristics of the beam with the collimator.

The effect of the collimator was to get a very small spot at the position of the first grating. Another effect, which is predictable, was that the number of positrons was diminished compared to before. This is obvious because the positrons outside 1 mm from the center of the collimator were removed from the beam. However, the number of positrons was still sufficient to conduct the experiment of interferometry (better explained in Sec. 0).

With the presence of the collimator the changing of the focalization voltage did not change considerably the dimension of the beam at the center of the chamber.

3.3. Effect of focalization potential

One parameter which is very crucial and must be chosen with particular attention is the potential of the tube 10. This is the focalization potential. Changing this potential, the position at which the beam is focalized is changed. To have good statistics during the experiment, it is preferrable a great number of positrons at the emulsion detector. However, also a tiny spot (below 3 mm in diameter, which is the dimension of the gratings) is desirable; these two conditions are not always related, so there is the need of a trade-off. This is represented by the density of positrons per unit area. This is the parameter to be maximized to improve the statistics for the interferometric experiment.

Three different scenarios are presented:

1- One can focalize the beam at the first grating (position 1). In this way the beam results to be very tiny in this position, but after that it diverges very rapidly and become very broad at the emulsion (position 2). This is not good, since it increases the incoherence of the primary beam and the spot area. Therefore, the density of positrons at the emulsion detector decreases. Moreover, some of the positrons can go outside the second grating (they do not interfere).
2- One can focalize at the emulsion (position 2). In this way it is obtained a tiny beam at the detector. But the con is that the beam is not focalized and so very broad at the beginning of the chamber, where the collimator is placed. The collimator acts as a geometrical filter and remove the great majority of the positrons. This is not good, because a lot of positrons are lost.
3- One can focalize at the middle of the interferometer, in a sort of trade-off between the scenarios described before. In this way the beam is quite collimated throughout all the interferometer, in the sense that it doesn't diverge too much. The effect is that the density of positrons increases at the detector.

The best solution is the third scenario. In order to choose the desired potential, a series of measurement were performed. Data are summarized in Table 3.4.

V_F (kV)	$FWHM_x$ (mm)	$FWHM_y$ (mm)	$\#\ of\ spots\ for\ 400\ frames$	$density$ ($\#\ of\ spots/mm^2$)
6.5	3.22	3.12	2737	329.6
7	3.27	2.83	3304	345.7
7.25	3.70	3.02	3722	357.2
7.5	4.08	3.27	4291	417.1
7.75	4.20	3.25	5340	402.1
8	5.29	3.90	6578	360.6
8.5	8.55	6.42	12045	239.3

Table 3.4: characteristics of the beam with different focalization potentials.

The number of spots as a function of the focalization potential is presented in Table 3.4. As you can see, the number of positrons at the detector position was maximized for the higher voltage. However, it is possible to notice that also the dimensions of the spot increased markedly (8.55 mm and 6.42 mm along x and y respectively), as if the focalization happened earlier and earlier (scenario 1). Plotting the density of positrons per unit area (Figure 3.3), it is possible to observe an interesting thing. The better condition in term of density was around 7.5-7.8 kV. This seems the potential described in scenario 3, where the focalization happened at an intermediate position between the first grating and the detector. Around this potential it was chosen the one that will be used for the experiment.

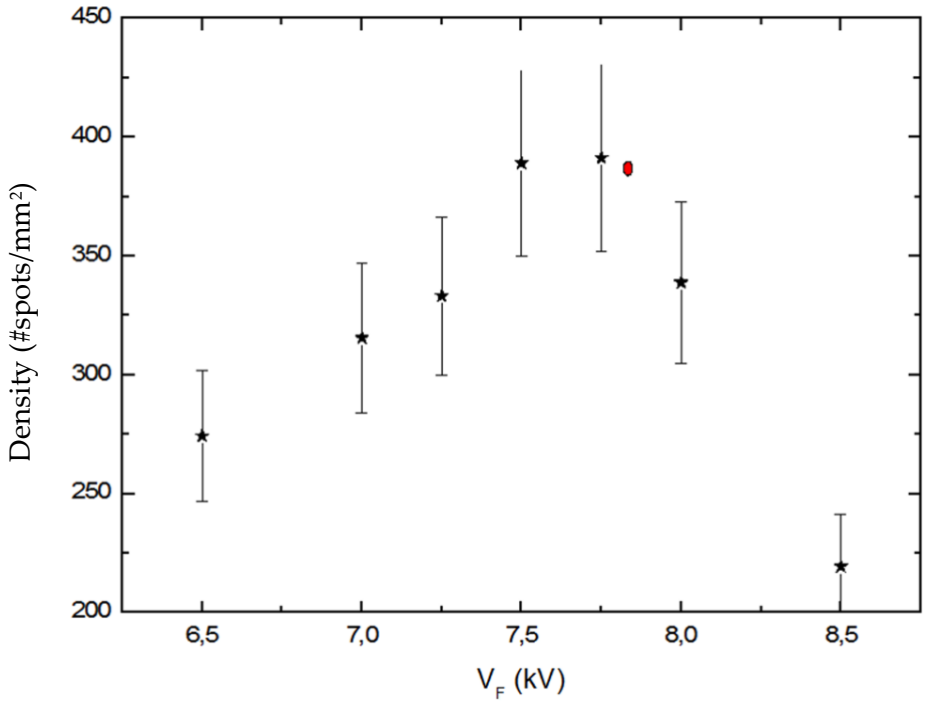

Figure 3.3: plot of the spot density for different focalization potentials.

From the figure, the red dot was chosen as reference. This corresponds to 7.8 kV. This was chosen because it is in the region of best density, but slightly above 7.5 kV and so a higher number of positron and higher dimension of the spot is expected.

In Table 3.5 are summarized the parameter chosen for the experiment and the correspondent dimension of the spot at the center of the chamber and at the end of the interferometer. Starting from around 1.5 mm of FWHM, it ends up being around 4 mm at the end of the interferometer. The number of positrons per second is around 10^2 (explained in the next section).

E (keV)	V_F (kV)	$FWHM_x$ (mm) at position 1	$FWHM_y$ (mm) at position 1	$FWHM_x$ (mm) at position 2	$FWHM_y$ (mm) at position 2	e^+/s
14	7.8	1.22	0.90	4.20	3.25	$\sim 2 \cdot 10^2$

Table 3.5: "final" parameters of the beam.

3.4. Number of positrons

The number of positrons is a fundamental parameter to be considered. This impact the statistics and therefore the capability of observing an interference pattern at the detector. So, the number of positrons expected to reach the detector is used to estimate the time of exposure needed for conducting the experiment.

A first estimation of the number of positrons was conducted using the MCP and is reported in the tables of the previous sections. Starting from the total spot revealed by the camera during the acquisition, it was possible to retrieve the number of positrons. Indeed, knowing the exposure time, an estimation of the number of spots per second was obtained; then, recalling Figure 2.40, the detection efficiency is around 50% for positrons at 14keV. Therefore, multiplying the number of spots per second by two, an estimation of the number of positrons per second was obtained.

To summarize, at the beginning the number of positrons per second was $5 \cdot 10^3$, which became 10^3 after the collimator (~80% loss). Now, estimating that every grating "kills" half of the positrons (~90% loss) [20], the conclusion is that at the detector $\sim 2 \cdot 10^2$ positrons per second are expected.

To acquire sufficient statistics, there is the need of $3 - 4 \cdot 10^7$ grains in the analysis region [2]. Therefore, the time needed for a single exposure is around $2 \cdot 10^5$ seconds, which means around 2 days.

3.5. Beam alignment

An important step is the alignment of the beam with the optical axis of the interferometer. To do this, a laser of reference has been used. It is a He-Ne laser placed at ~5 m from the chamber. The heigh of the laser was made to coincide with the center of the chamber. Then, the laser had two degrees of freedom: they allowed to correct the direction of the laser beam both in x and y.

Using the MCP the bright spot left (indirectly) by the positrons was clearly visible also at naked eye (Figure 3.4). The protocol consisted in using special glasses, whose lenses act as filters. In this way the spot of the laser resulted visible only in its brightest part, which was sub-millimetric. Changing the free parameters of the laser, the spot of the laser was aligned with the one left by the positrons on the MCP. In this way it was known exactly where the beam was and propagated.

After having in mind all these things – dimension of the spot at the chamber center, number of positrons, position of the beam – the interferometer could be mounted.

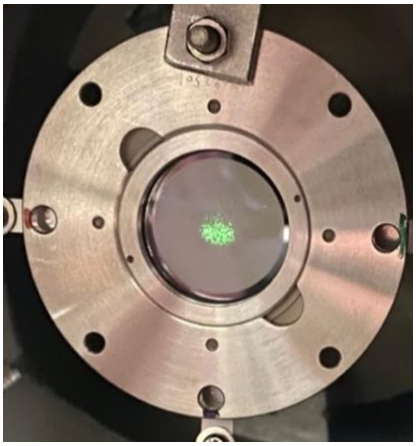

Figure 3.4: image of the spot left by positrons on the phosphor screen of the MCP.

The interferometer has two degrees of freedom and is supported by a system with a bellow. This bellow allows the interferometer to be tilted (Figure 3.5). The alignment with the beam (and the laser) consisted in modifying the interferometer orientation until the optical axis coincides with the laser beam. To do this in practice, a spot with a red pen in the center of the interferometer chamber was drawn. Then, the position of the interferometer was corrected until the red point and the laser spot coincided. This was a first alignment; a more accurate one was conducted with the MCP.

The MCP was mounted the end of the interferometer: the position that will host the emulsion detector. The strategy was then to align the laser with the spot on the MCP (moving the interferometer). Once done this, the optical axis of the interferometer was aligned with the positron beam.

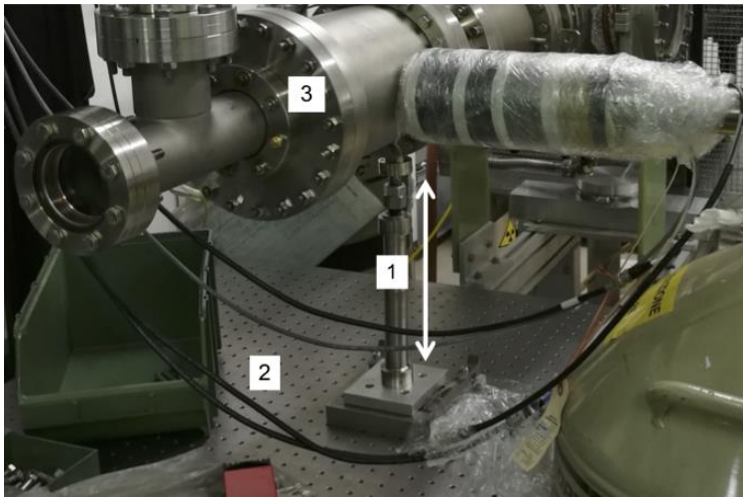

Figure 3.5: image of the system (1) to adjust the orientation of the interferometer (3), mounted on a support (2).

4 Preliminary results

4.1. First set of measurements

A series of measurements were performed with the setup prepared and described previously. In particular, 3 measurements were performed with 3 different exposure times. This can give useful information about the different exposure times.

To perform the measurements, the emulsion detector has to be installed on its support and inserted in the chamber. This process is delicate because it has to be performed in a condition of full darkness. Indeed, every light source can spoil the measurement, creating noise onto the emulsion. In this phase, every light source of the laboratory was dimmed with extreme care. Only with a dim red light mounted on the head, it was possible to proceed mounting the emulsion on the support and inserting the support on its rail inside the chamber.

After that, the chamber was closed and the vacuum was made. After 20 hours the vacuum reached $\sim 10^{-6}\ mbar$ of pressure; the potentials of the optics were set, the positrons started arriving and the measurement began. A HPGe detector was placed in the position of the emulsion to keep monitored the experiment during its course.

In Table 4.1 the characteristics of the 3 experiments are presented.

	***Emulsion* 1**	***Emulsion* 2**	***Emulsion* 3**
exposure time (hours)	8	24	64
Pressure (mbar)	$\sim 10^{-6}$	$\sim 10^{-7}$	$\sim 10^{-7}$

Table 4.1: characteristics of the three emulsions taken.

4.1.1. Results

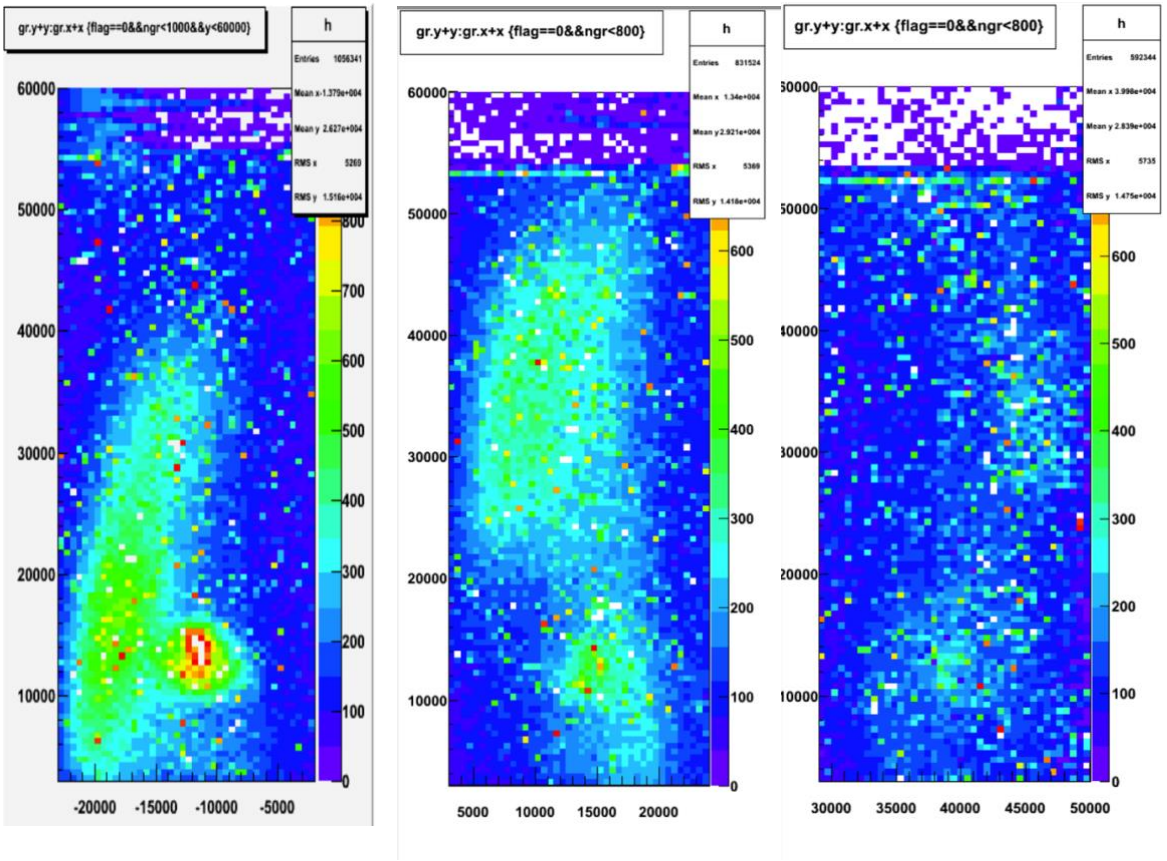

Figure 4.1: image of the signal on the three emulsions (8h left, 24h middle, 64h right).

In all the measurements unexpected things happened. First of all, a second big signal, besides the right spot, appears as a coma. It is clearly visible in Figure 4.1. Secondly, this strange signal seems to move during the measurements. In conclusion, due to these problems, a lot of positrons "went" into the coma and so the statistic of the central spot was reduced. The periodicity results to be not clear in the central spot. The system has to be reviewed in order to understand what happened.

After a check of all the setup, it was possible to notice that the second grating was broken in the lower right corner. Therefore, many positrons came out of the hole creating the second signal.

The second grating was suddenly substituted and the interferometer was re-aligned before proceeding with a second series of measurements.

4.2. Second set of measurements

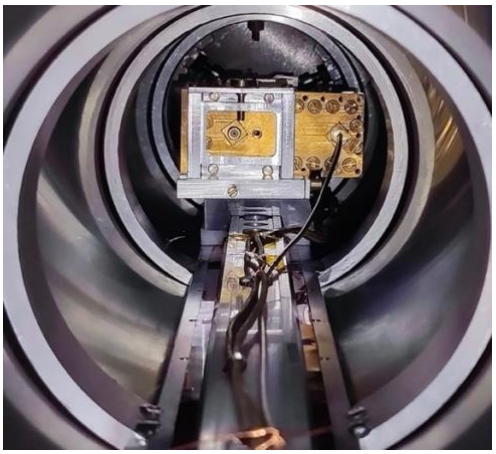

Figure 4.2: view of the microwave modulus from the end of the chamber.

For the second set of measurements the modulus of microwave was installed in the chamber, constituting a step forward with respect to the previous setting (Figure 4.2). Moreover, the microwave field was kept off during the first measurement, in order to reproduce the interferometric experiment without any perturbation (looking for an improvement with respect to the first set of measurements). Then, in the two successive measurements the microwave field was turned on. Some critical values of the electric field were chosen, as shown in orange in Figure 4.3, in order to observe the oscillating behavior of visibility (the so-called revival) predicted by theory (Sec. 1.5). In particular, 22 dB and 26 dB of attenuation were chosen to reproduce 0.5 mW and 0.23 mW of power respectively. In Table 4.2 are presented the characteristics of this set of measurements.

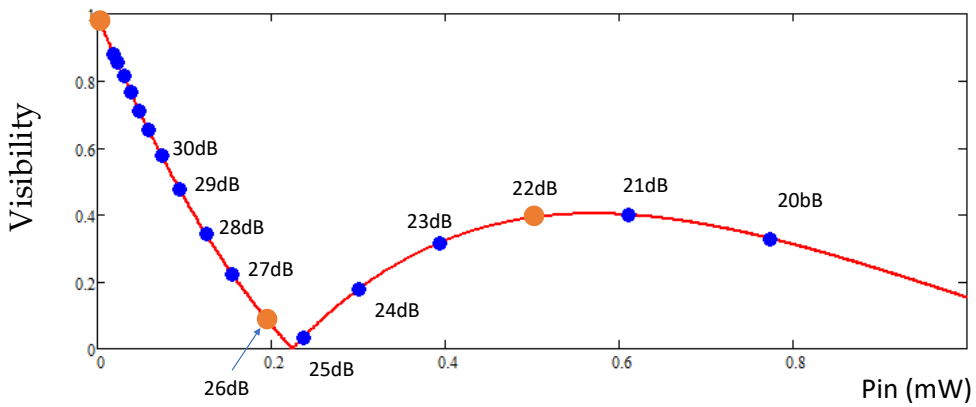

Figure 4.3: sketch of the three points (orange) of microwave field power chosen for the experiment.

	***Emulsion* 1**	***Emulsion* 2**	***Emulsion* 3**
exposure time (hours)	48	48	48
Pressure (mbar)	$\sim 10^{-6}$	$\sim 10^{-6}$	$\sim 10^{-6}$
Microwave field power (mW)	0	0.23	0.5

Table 4.2: characteristics of the three emulsions taken.

4.2.1. Results

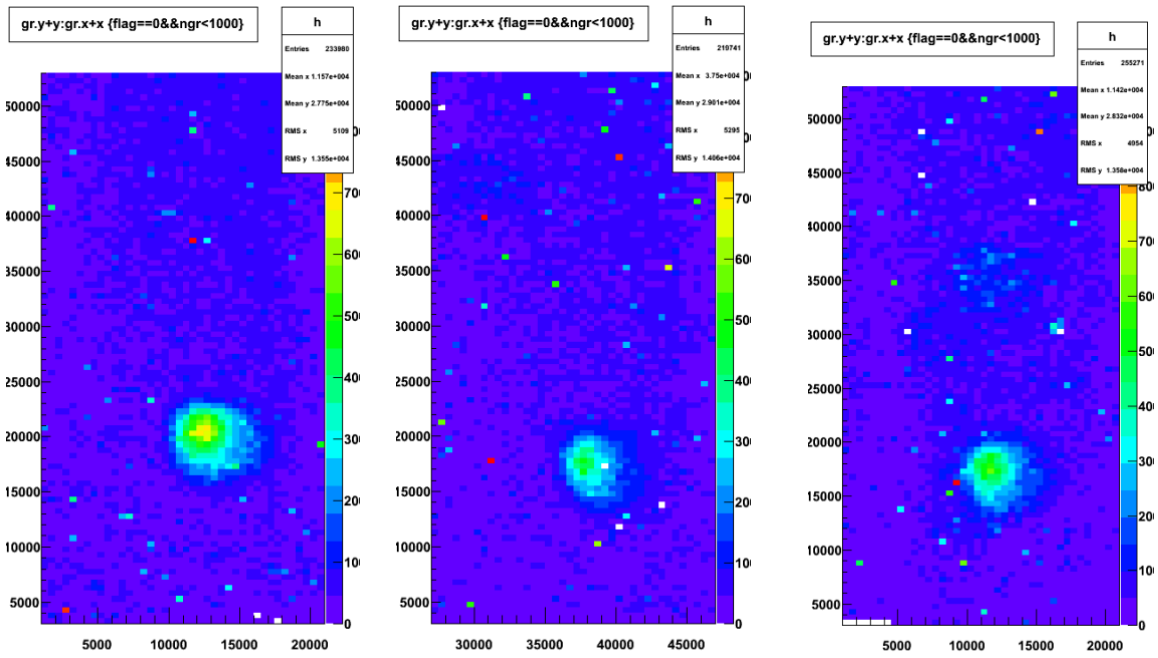

Figure 4.4: image of the signal on the three emulsions.

As reported in Figure 4.4, the signal on the emulsion is clearly visible and results in a single central spot (as expected). Therefore, an improvement with respect to the first set of measurements is evident.

From the analysis performed using the Rayleigh test, in all the emulsions it results that the periodicity is still not visible. The results show that for a future campaign of measurements is necessary to increase the statistics and to improve the vacuum level. A pressure equal or smaller than $10^{-7}\ mbar$ is desirable to conduct the experiment. Indeed, a bad vacuum means a higher probability of scattering between positrons and other particles. Scattering makes the particle-wave losing coherence

[24]. The loss of coherence, as already explained during Sec. 2.4, is not good for this experiment. That is why a better level of vacuum is necessary for a future measurement.

5 Conclusions

During the thesis work a series of milestones have been achieved in order to carry out the *Quantum revival* experiment. Here are synthetized the main achievements:

- Thermal treatment of the moderator. This resulted important to improve the number of monochromatic positrons coming to the interferometer.
- Optimization of the transport condition of positrons. This stage consisted in optimizing the potentials of the electrostatic optics in order to improve the quality of the beam. Thanks to a real time monitoring using the MCP, it was possible to have a better characterization of the positron beam and to optimize the dimension of the spot and the number of positrons per second. The experimental setup has been improved with respect to the first QUPLAS-0 experiment.
- Periodicity test on the emulsions. This tested the suitability of the emulsion detector for the experiment.
- Implementation of the interferometer. This consisted in mounting every component of the interferometer, arranging the longitudinal and rotational alignment of the two gratings.
- First campaign of measurements. This step provided important information for future improvements of the setup and for future measurements.

In conclusion, the experiment is at an advanced stage for its implementation. Soon, the plan will be to improve the vacuum level and to increase the statistics of measurement.

Bibliogaphy

[1] https://sites.google.com/site/positronlaboratoryofcomovepas/visit-the-positron-laboratory/quplas.

[2] S. Sala, A. Ariga, A. Ereditato, R. Ferragut, M. Gianmarchi, M. Leone, C. Pistillo, P. Scampoli. **First demonstration of antimatter wave interferometry**. Science Adv. 5 EAAV7610 (2019).

[3] J. Audretsch, V. D. Skarzhinsky. **Quantum Processes beyond the Aharonov-Bohm Effect**. Found. Phys. 28, 777–788 (1998).

[4] A. Kostelecky. **The status of CPT**. IUHET **397**. (1998).

[5] J. W. Cronin. **Report of the Working Group on CP Violation and Rare Decays**. University of Chicago (1984).

[6] A. Einstein. **Die Grundlage der allgemeinen Relativitätstheorie**. Ann. Phys. **354**, 769–822 (1916).

[7] B. Heckel et al. **Results on the strong equivalence principle, dark matter, and new forces**. Adv. Space Res. 1225– 1230 (2000).

[8] C. D. Anderson. **The positive electron**. Phys. Rev. **43**:491, (1933).

[9] E. Schrödinger. **Quantisierung als Eigenwertproblem**. Ann. Phys. **384**, 361–376 (1926).

[10] A. Einstein. **Zur Elektrodynamik bewegter Körper**. Ann. Phys. **322**, 891–921 (1905).

[11] P. A. M. Dirac. **A Theory of Electrons and Protons**. Proc. R. Soc. Lond. A **126**, 360–365 (1930).

[12] T. Young. **The Bakerian Lecture: On the Theory of Light and Colours**. Philos. Trans. R. Soc. Lond.**92**, 12–48 (1802).

[13] A. H. Compton. **A Quantum Theory of the Scattering of X-rays by Light Elements**. Phys. Rev. **21**, 483–502 (1923).

[14] P. G. Merli, G. F. Missiroli, and G. Pozzi. **On the statistical aspect of electron interference phenomena**. Am . J. Phys. **44**, (1976).

[15] M. Born and E. Wolf. Principles of Optics. **Electromagnetic Theory of Propagation, Interference and Diffraction of Light**. Cambridge University Press, (1999).

[16] J. Goodman**. Introduction to Fourier optics**. Roberts and Company Publishers, (2004).

[17] R. Tumulka, A. Viale, and N. Zangi. **Reduced coherence in double-slit diffraction of neutrons**. Phys. Rev. *A* **75**, (2007).

[18] A. S. Sanz, F. Borondo, and M. J. Bastiaans. **Loss of coherence in double-slit diffraction experiments**. Phys. Rev. *A* **71**, (2005).

[19] R. Bonifacio and S. Olivares. **Young's experiment, schrödinger spread and spontaneous intrinsic decoherence**. Z. Naturforsch. **56**, 41–47 (2001).

[20] S. Sala, M. Gianmarchi, S. Olivares. **Asymmetric Talbot-Lau Interferometry for inertial sensing**. Phys. Rev. A **94**, 033625 (2016).

[21] E. Lau. **Beugungserscheinungen an doppelrastern**. Ann. Phys. **437,** 417–423 (1948).

[22] K. Oberthaler, S. Bernet, E. M. Rasel, J. Schmiedmayer, A. Zeilinger. **Inertial sensing with classical atomic beams**. Phys. Rev. A **54**, 3165–3176 (1996).

[23] S. Sala et. al., **Matter-wave interferometry: towards anti-matter interferometers**. J. Phys. B: At. Mol. Opt. Phys. **48**, 195002 (2015).

[24] S. Cialdi et. al. **The QUPLAS quantum revival experiment** (to be submitted).

[25] M. S. Chapman et. al. **Photon Scattering from Atoms in an Atom Interferometer: Coherence Lost and Regained.** Massachusetts Institute of Technology, (1995).

[26] M. S. Chapman. **Photon Induced Coherence Loss in Atom Interferometry**. Massachussets Institute of Technology, (1995).

[27] A. Ariga, S. Cialdi, G. Costantini, A. Ereditato, R. Ferragut, M. Gianmarchi, M. Leone, G. Maero, L. Miramonti, C. Pistillo, M. Romé, S. Sala, P. Scampoli, V. Toso. **The QUPLAS experimental apparatus for antimatter interferometry**. Nucl. Instrum. Methods Phys. Res A **951**, 163019 (2020).

[28] D.M. Chen, K.G. Lynn, R. Pareja, B. Nielsen. **Measurement of positron reemission from thin single-crystal W(100) Films**. Phys. Rev. B **31**, (1985).

[29] A. Zecca, L. Chiari, A. Sarkar, S. Chattopadhyay, M. J. Brunger, **Procedures for conditioning W and Ni-moderators for application in positron-scattering measurements.** Nucl. Instr. & Meth. in Phys. Res. B **268**, (2010).

[30] G. Tosi. **Produzione di positronio in materiali porosi per l'esperimento Aegis sull'antimateria al CERN**. Tesi di Laurea in Fisica. Università degli studi di Milano. (2010-2011).

[31] https://www.thorlabs.com/index.cfm.

[32] https://ecatalog.mitutoyo.com/Linear-Scales-ABS-AT715-Series-539-Slim-Spar Type-C1281.aspx.

[33] L. Anzi, A. Ariga, A. Ereditato, R. Ferragut, M. Giammarchi, G. Maero, C. Pistillo, M. Romé, P. Scampoli, V. Toso. **Sensitivity of emulsion detectors to low energy positrons**. JINST **15**, P03027 (2020).

[34] S. Aghion, A. Ariga, T. Ariga, M. Bollani, E. Dei Cas, A. Ereditato, C. Evans, R. Ferragut, M. Giammarchi, C. Pistillo, M. Romé, S. Sala, and P. Scampoli. **Detection of low energy antimatter with emulsions**. JINST **11,** P06017 (2016).

[35] V. J. Ghosh, D. O. Welch, and K. G. Lynn. **Monte carlo studies of positron implantation in elemental metallic and multilayer systems**. AIP Conf. Proc. **303**(1), 37–47 (1994).

[36] G.C. Aers, P.A. Marshall, T.C. Leung, and R.D. Goldberg. **Defect profiling in multilayered systems using mean depth scaling**. Appl. Surf. Sci. **85**, 196–209 (1995).

[37] T. A. Savas, M. L. Schattenburg, J. M. Carter, and Henry I. Smith. **Large-area achromatic interferometric lithography for 100 nm period gratings and grids**. J. Vac. Sci. Technol. B, Microelectron. Nanometer. Struct. Process. Meas. Phenom. **14**(6), 4167–4170 (1996).

[38] S. Aghion, A. Ariga, M. Bollani, A. Ereditato, R. Ferragut, M. Giammarchi, M. Lodari, C. Pistillo, S. Sala, P. Scampoli, and M. Vladymyrov**. Nuclear emulsions for the detection of micrometric-scale fringe patterns: an application to positron interferometry**. JINST **13**, P05013 (2018).

[39] S. Sala. **QUPLAS: towards antimatter interferometry**. Tesi di dottorato in Fisica, Astrofisica e Fisica Applicata. Università degli studi di Milano. (2018)

[40] G. F. Knoll. **Radiation Detection and Measurement**. 4ª ed. John Wiley & Sons, Inc.. 365–463 (2010).

[41] G. Vinelli, R. Ferragut, M. Giammarchi, G. Maero, M. Romé and V. Toso. **Real time monitoring of a positron beam using a microchannel plate in single-particle mode**. JINST **15** P11030 (2020).

[42] M. Dapor, A. Miotello and D. Zari. **Montecarlo simulation of positron stimulated secondary electron emission from solids**. Phys. Rev. B **61** (2000).

List of Figures

List if Tables